TFAP2 paralogs pioneer chromatin access for MITF and directly inhibit genes associated with cell migration

Colin Kenny[1], Ramile Dilshat [2], Hannah Seberg[1+], Eric Van Otterloo[1]*, Gregory Bonde[1], Annika Helverson[1], Eiríkur Steingrímsson[2], Robert A. Cornell[1, #]

1. Department of Anatomy and Cell Biology, College of Medicine, University of Iowa, Iowa City, Iowa

2. Department of Biochemistry and Molecular Biology, BioMedical Center, Faculty of Medicine, University of Iceland, Sturlugata 8, 101 Reykjavik, Iceland

[+] Current address: University of Manchester

* Current address: Iowa Institute for Oral Health Research, Department of Anatomy and Cell Biology, Department of Periodontics, College of Dentistry, University of Iowa, Iowa City, Iowa

[#]Corresponding author:

Robert-cornell@uiowa.edu, 319-335-8908

Conflict of interest statement: CK, RD, HS, EVO, GB, AH, ES and RAC declare no conflicts of interest.

Key words: MITF, TFAP2A, TFAP2C, chromatin, nucleosome, pioneer factor, transcriptional activation, repression.

Abstract

Transcription factors in the Activating-enhancer-binding Protein 2 (TFAP2) family redundantly regulate gene expression in melanocytes and melanoma. Previous ChIP-seq experiments indicate that TFAP2A and Microphthalmia-associated Transcription Factor (MITF), a master regulator in these cell types, co-activate enhancers of genes promoting pigmentation. Evidence that TFAP2 paralogs can serve as pioneer factors supports the possibility that TFAP2 facilitates MITF binding at co-bound enhancers, although this model has not been tested. In addition, while MITF and TFAP2 paralogs both appear to repress genes that promote invasion, whether they do so by co-repressing enhancers is unknown. To address these questions we evaluated gene expression, chromatin accessibility, TFAP2A and MITF binding, and chromatin marks characteristic of active enhancers in SK-MEL-28 melanoma cells that were wild-type or deleted of the two *TFAP2* paralogs with highest expression, *TFAP2A* and *TFAP2C* (i.e., *TFAP2*-KO cells). Integrated analyses revealed distinct subsets of enhancers bound by TFAP2A in WT cells that are inactivated and activated, respectively, in *TFAP2*-KO cells. At enhancers bound by both MITF and TFAP2A, MITF is generally lost in *TFAP2A/TFAP2C* double mutants, but not vice versa, implying TFAP2 pioneers chromatin access for MITF. There is a strong correlation between the sets of genes inhibited by MITF and TFAP2, although we did not find evidence that TFAP2 and MITF inhibit enhancers cooperatively. The findings imply that MITF and TFAP2 paralogs cooperatively affect the melanoma phenotype.

Introduction

Gene expression in developing melanocytes and melanoma, a cancer derived from the melanocyte lineage, is regulated by transcription factors including Microphthalmia-associated transcription factor (MITF) and members of the SOXE, PAX and TFAP2 families (Atchison, 2014; Betancur et al., 2010; Eckert et al., 2005; Goding, 2000; Hartman and Czyz, 2015; Hoek et al., 2008b; Mollaaghababa and Pavan, 2003; Seberg et al., 2017a; Strub et al., 2011; Van Otterloo et al., 2010; Van Otterloo et al., 2012). MITF is required for differentiation of melanocytes during development, and its activity is regulated at both the transcriptional and post-

translational levels (Rambow et al., 2019). In melanoma cells, high levels of MITF activity promote cell proliferation and pigmentation, while lower levels promote an invasive phenotype (Carreira et al., 2006; Rambow et al., 2019). Mass spectroscopy revealed that MITF interacts with components of both the PBAF chromatin remodeling complex, including BRG1 and CDH7, and the NURF remodeling complex, including RBBP4 (de la Serna et al., 2006; Laurette et al., 2015). Furthermore, chromatin immunoprecipitation of BRG1 in cells depleted of *MITF* revealed that MITF recruits BRG1 to the promoters of specific genes, including *TYR*, which encodes the rate-limiting enzyme in melanin synthesis Tyrosinase (Laurette et al., 2015). Similar analysis suggested that SOX10 also recruits BRG1 to chromatin, and at some loci it does so in co-operation with MITF (Laurette et al., 2015). Conversely, there is evidence that PAX3 inhibits the activity of MITF at the *DCT* promoter (Lang et al., 2005). Furthermore, low MITF activity is associated with an invasive phenotype, and deletion or knockdown of *MITF* results in upregulation of genes that promote migration and invasion (Dilshat et al., 2021). MITF CUT&RUN peaks are found near some genes whose expression is upregulated in *MITF* mutant cells, implying MITF directly represses their expression (Dilshat et al., 2021).This set of MITF peaks is enriched for the binding site of FOXC1, a transcriptional repressor (Du et al., 2012), suggesting MITF has co-factors in its repressive function as well as its activating one.

The activating enhancer-binding family of transcription factors, comprising five members, TFAP2A-E, regulate development of many cell types and organs including neural crest, placodes, epidermis, trophectoderm, heart, kidney, and brain (Bamforth et al., 2001; Brewer et al., 2002; Knight et al., 2003; Kuckenberg et al., 2012; Luo et al., 2002; Mitchell et al., 1991; Moser et al., 1997; Schorle et al., 1996; Tan et al., 2008; Wang et al., 2006). In several contexts, including melanocyte differentiation, TFAP2 paralogs function redundantly (Kołat et al., 2021; Li and Cornell, 2007; Van Otterloo et al., 2010; Wang et al., 2008). For instance, in zebrafish *tfap2a* loss-of-function mutant embryos the number of melanocytes is lower than normal and pigmentation is profoundly delayed relative to in wild type embryos; this phenotype is exacerbated if *tfap2a* mutant embryos are also depleted of *tfap2e* expression with antisense morpholinos (Van Otterloo et al., 2010). In zebrafish melanoma Tfap2a and Tfap2e also appear to act redundantly to promote proliferation and, interestingly,

to suppress cell adhesion and cell migration (Campbell et al., 2021). Consistent with redundant function of Tfap2 paralogs in the melanocyte lineage, in the skin of mouse embryos with neural-crest specific knockout of the two paralogs with highest expression, *Tfap2a* and *Tfap2b*, there are fewer-than-normal cells expressing markers of melanocytes (Seberg et al., 2017b).

Tfap2 paralogs and MITF appear to co-activate certain genes. For instance, in a human melanoma cell line, the *in vitro* enhancer activity of an element within an *IRF4* intron depended on the simultaneous binding of MITF and TFAP2 (Praetorius et al., 2013). Further, in zebrafish *tfap2a* and *mitfa* double mutant embryos there is a greater-than-additive reduction in the number, and level of pigmentation, of melanocytes in comparison to in single mutants (Seberg et al., 2017b). Evidence that Tfap2 paralogs and Mitfa operated in parallel, rather than Tfap2 paralogs functioning upstream of *mitfa* expression, is that in *tfap2a/tfap2e* doubly-depleted zebrafish embryos, *mitfa* expression, and the number of *mitfa*-expressing cells, are not significantly changed from *tfap2a* singly depleted embryos (Seberg et al., 2017b). Supporting parallel activity of Tfap2 paralogs and MITF, the promoters of MITF target genes are enriched for TFAP2 consensus binding sites (Laurette et al., 2015; Rambow et al., 2015). Moreover, ChIP-seq experiments in primary melanocytes suggest that TFAP2A and MITF bind overlapping regions of chromatin near genes encoding regulators of pigmentation (Seberg et al., 2017b). Collectively, these observations indicate that TFAP2 paralogs co-activate a subset of MITF target genes by binding at the same enhancers. Still unclear, however, is whether they also co-repress enhancers, and whether TFAP2 paralogs and MITF act cooperatively or independently at enhancers they co-regulate.

TFAP2 paralogs may serve as pioneer factors for MITF, although not all evidence supports this possibility. *Pioneer* or *initiating* TFs can bind nucleosome-bound DNA and recruit other TFs that lack this property called *settler TFs* (reviewed in Voss and Hager, 2014; Zaret, 2020; Zaret and Carroll, 2011). Evidence that TFAP2 paralogs are pioneer factors includes, first, that TFAP2 binding site is over-represented within DNase1-protected “footprints” in mouse embryonic stem cells induced to differentiate (Sherwood et al., 2014). Second, TFAP2A catalyzes assisted loading of androgen receptor (AR) in epididymis cells (Pihlajamaa et al., 2014) and estrogen receptor in

MCF-7 cells (Tan et al., 2011). Third, the TFAP2 binding site is enriched for at the center of ATAC-seq peaks, implying it has a strong effect on chromatin accessibility (Grossman et al., 2018). Fourth, ATAC-seq peaks in naïve-stated human ESC showed reduced openness in TFAP2C KO cells (Pastor et al., 2018), and forcing expression of TFAP2C in human ESC is sufficient to open chromatin at loci where it binds (Li et al., 2019). Finally, TFAP2A, TFAP2B and TFAP2C can bind nucleosomes (Fernandez Garcia et al., 2019). Together these findings support the possibility that TFAP2 displaces nucleosomes and thereby facilitates chromatin binding by MITF. However, it not clear that MITF needs a pioneer factor to bind chromatin. In the *dynamic-assisted-loading model*, all classes of TFs have short residency on chromatin (reviewed in Voss and Hager, 2014). *Initiating TFs* are able to recruit ATP-dependent chromatin remodelers (nBAF, SWI/SNF, INO80, ISWI, NURD) and thereby make chromatin accessible to other TFs, i.e., the *assisted* TFs (Swinstead et al., 2016b). As mentioned above, MITF binds various components of the SWI/SNF complex (Aras et al., 2019; de la Serna et al., 2006; Keenen et al., 2010) and the chromatin remodeler CHD7 (Laurette et al., 2015) and so meets the criteria for an initiating factor. If the dynamic-assisted-loading model holds in this situation, MITF would have no need for a pioneer factor like TFAP2 to assist its binding to chromatin.

To address these questions, we systematically tested the effect of loss of TFAP2 paralogs on: nucleosome positioning, using the assay for transposase-accessible chromatin using sequencing (ATAC-seq) methodology; enhancer activity, using cleavage under targets and release using nuclease (CUT&RUN) with anti-H3K27Ac, anti-H3K4me3, and anti-H3K27me3; and binding of MITF, using CUT&RUN. We similarly assessed binding of TFAP2A in cells harboring loss of function mutations in *MITF*. Our results support the notion that TFAP2 factors behave like the canonical pioneer factor FOXA1: at many chromatin elements bound by TFAP2A, loss TFAP2 led to loss of enhancer activity, and in a large subset, it also let to chromatin becoming condensed. In both of these subsets of TFAP2-activated enhancers, MITF binding was TFAP2 dependent. In addition, we find evidence that TFAP2 paralogs can also inhibit enhancers, and at a subset of those that they inhibit, they exclude binding of MITF. Finally, the analyses suggest TFAP2 directly inhibits many of the same genes that MITF inhibits, but we do not find evidence that TFAP2 and MITF

co-repress the same enhancers. Together these findings illuminate the mechanisms by which TFAP2 and MITF coordinately regulate differentiation of melanocytes and the phenotype of melanoma cells.

Results

Tfap2a and Tfap2e redundantly promote the differentiation of zebrafish embryonic melanocytes

We first sought to use a zebrafish mutant to confirm an earlier conclusion based on morpholino-mediated knockdown that Tfap2 paralogs redundantly promote differentiation of embryonic melanophores. In the melanocyte lineage of zebrafish embryos, levels of *tfap2e* expression are high, those of *tfap2a* and *tfap2c* are lower (~30% of the level of *tfap2e*), and those of *tfap2b* are negligible (Higdon et al., 2013). We previously reported that wild-type (WT) embryos injected with antisense morpholino oligonucleotides (MO) targeting the splicing of *tfap2e* exhibit no overt phenotype, but embryos homozygous for a *tfap2a* loss-of-function allele (i.e., lockjaw , Knight et al., 2003), injected with the *tfap2e* MO have fewer embryonic melanocytes than counterparts injected with a non-targeting control MO, and pigmentation is delayed in them, although it occurs eventually (Van Otterloo et al., 2010). To confirm that the recovery of pigmentation did not simply reflect the transient effects of the *tfap2e* morpholino we used zinc-finger nucleases to engineer zebrafish lines harboring frame-shift-inducing mutations in *tfap2e* (details in **Supplemental Fig. S1A-B)**. qPCR analysis showed that expression of the *tfap2e* transcript was significantly lower in *tfap2e* mutant than in WT embryos, suggesting nonsense-mediated decay (**Supplemental Fig. S1C**)**.** As in embryos injected with *tfap2e* MO, there was no overt phenotype in homozygous *tfap2e* mutants (**Supplemental Fig. S1D-F**). However, in *tfap2a*/*tfap2e* double mutants the number of melanocytes was significantly reduced in the dorsal stripe at 29 hours post fertilization (hpf) relative to those in *tfap2a* single mutants. At this stage these cells were under-pigmented relative to in non-mutant siblings, although their pigmentation reached wild-type levels by 48 hpf (**Fig. 1A-E; Supplemental Fig. S1G-J**). In summary, the reduction in melanocyte number and delay in pigmentation in *tfap2a/tfap2e* double mutant versus WT embryos implies that TFAP2 paralogs promote melanocyte proliferation and differentiation in a redundant fashion.

TFAP2A binds open and closed chromatin

We next sought to learn TFAP2 paralogs interact with MITF in activating and repressing gene expression in a single cell line. We have reported the genes differentially expressed between SK-MEL-28 melanoma cells that are WT or harboring loss-of-function mutations in all alleles of MITF, as well as binding of MITF using cleavage under targets and release under nuclease (CUT&RUN) (Dilshat et al., 2021). Here, again using SK-MEL-28 melanoma cells, we carried out (1) CUT&RUN using antibodies to TFAP2A (i.e., TFAP2A peaks), (2) CUT&RUN using antibodies to chromatin marks indicative of active regulatory elements (H3K27Ac and H3K4Me3) (Creyghton et al., 2010; Pekowska et al., 2011), and of inactive chromatin (H3K27Me3) (Ringrose and Paro, 2004), and (3) ATAC-seq to distinguish between open and closed chromatin (Buenrostro et al., 2013). We used IgG as a background control and the MACS2 software to call peaks in each dataset (**Supplemental Fig. S2A-B**). Based on proximity to transcriptional start sites (TSS), about one-third of TFAP2A peaks appeared to be at or near promoters (within 3 kb of a TSS). As expected, these elements had strong H3K4Me3 signal (**Supplemental Fig. S2B**). At promoter-proximal TFAP2A peaks, the H3K27Ac signal in WT cells was relatively consistent, whereas at promoter-distal TFAP2A peaks the H3K27Ac signal ranged from high to background level (**Supplemental Fig. S2B-C**). About two-thirds of TFAP2A peaks overlapped ATAC-seq peaks, indicating that they were in open chromatin (**Supplemental Fig. S2D-E**). Of note, the read depth (height) of a peak approximates the number of chromosome molecules where TFAP2A binds. The average read depth of the TFAP2A peaks in closed chromatin was only about 50% of that in open chromatin but was nonetheless 80-fold higher than the IgG background read depth (**Supplemental Fig. S2D-E, Supplemental Fig. S3A-B for example loci**). Importantly, the TFAP2 binding site was strongly enriched for in both TFAP2A-bound elements where the local ATAC-seq signal was called as a peak and in counterparts where it was not ($p < 1 \times 10^{-1785}$ and $p < 1 \times 10^{-4375}$, respectively), supporting the idea that TFAP2A binds DNA directly even when the DNA is occupied by nucleosomes (**Supplemental Fig. S3C-D**). These results indicate that TFAP2A binds at both open and closed chromatin, consistent with it being a pioneer factor, and at enhancers and promoters with a range of activity levels.

TFAP2A activates enhancers as in pioneer factor and non-pioneer factor modes

We next sought to identify enhancers and promoters that TFAP2 paralogs regulate directly, and, of these, the fraction that they regulate as pioneer factors. To these ends we used Crispr/Cas9 methods to introduce frame-shift mutations into the *TFAP2* genes with high expression in SK-MEL-28 cells, *TFAP2A* and *TFAP2C;* we then carried out RNA-seq, ATAC-seq, and CUT&RUN with antibodies to H3K27Ac, H3K4me3, and H3K27me3. In two independent knockout clones (hereafter, *TFAP2*-KO cells), Western blot analysis showed an absence of immunoreactivity for both proteins (**Supplemental Fig. S4A-E**). Control clones (hereafter WT cells) were derived from the parental SK-MEL-28 line transiently transfected with Cas9 but not with guide RNAs. RNA-seq revealed that expression of 532 genes was downregulated, and expression of 609 genes was upregulated, in *TFAP2*-KO cells (i.e., in both clones) versus in WT cells (**Supplemental Fig. S5A volcano plot**). We will refer to these sets as "TFAP2-activated genes" and "TFAP2-inhibited genes," respectively.

To identify candidates for enhancers directly activated by TFAP2 paralogs we first filtered TFAP2A peaks for those in chromatin that was open and active in WT cells (i.e., coinciding with peaks of ATAC-seq and H3K27Ac) (21,745/ 36,948 of TFAP2A peaks), then for those greater than 1 kb from a transcription start site (i.e., to filter out promoters) (11,005/ 21,745), and finally for those where the local H3K27Ac signal was significantly lower (adj $p < 0.05$, log2FC <-1) in *TFAP2*-KO cells relative to in WT cells (3,858/11,005).

To determine how often TFAP2 activates enhancers as a pioneer factor, at each directly TFAP2-activated enhancer we evaluated the ATAC-seq signal in WT and TFAP2-KO cells. At about half of the enhancers the ATAC-seq signal was also significantly lower (adj $p < 0.05$, log2FC <-1) in *TFAP2*-KO versus in WT cells (i.e., the ATAC-seq signal was TFAP2-activated) (**Fig. 2A, E-E'**); at this subset we infer that TFAP2 paralogs function as pioneer factors. At the remaining half, the ATAC-seq signal was unchanged between *TFAP2*-KO versus WT cells (i.e., the ATAC-seq

signal was TFAP2-independent) (**Fig. 2B, F-F'**); at this subset we infer that TFAP2 paralogs do not function as pioneer factors but rather as a transcriptional activator. Consistent with both subsets indeed being enhancers activated by TFAP2, both were associated with TFAP2-activated genes. Interestingly, the association was stronger for those where TFAP2 functions as a pioneer factor (**Fig. 2 I, J**) (**Table 1 and Table 2**). Moreover, at both subsets the H3K4me3 signal, which is associated with enhancer activity (Pekowska et al., 2011), was reduced in *TFAP2*-KO cells relative to in WT cells (**Fig. 2E'', F''**). While both subsets were strongly enriched for the TFAP2 binding site and certain other binding sites (e.g., RUNX), the subset pioneered by TFAP2 was more strongly enriched for the SOXE and MITF binding sites, while the non-pioneered subset was more strongly enriched for the FRA1, TEAD and the ZFX binding sites (**Fig. 2M, N**). Of note, FRA1 is a pioneer factor (Lee et al., 2018) which could explain why these elements do not depend on TFAP2 to be free of nucleosomes.

Table 1: Hypergeometric analysis: TFAP2 regulated enhancers and gene expression

Regulatory element (Enhancer)	Effect of TFAP2 on H3K27Ac	Effect of TFAP2 on ATAC	Effect of TFAP2 on RNA-seq	N (# of elements)	OR	LB	UB	p-value All DEG's	p-value |Log2FC| >1
-	Activates	-	Activates	3,838	2.36	2.06	2.70	2.8×10^{-33}	1.12×10^{-14}
-	Activates	-	Inhibits	3,838	1.03	0.85	1.24	7.0×10^{-01}	5.9×10^{-01}
-	Inhibits	-	Activates	1,304	1.23	0.93	1.60	1.24×10^{-1}	7.1×10^{-01}
-	Inhibits	-	Inhibits	1,304	2.30	1.87	2.82	4.95×10^{-14}	4.8×10^{-06}
Pioneered	Activates	Activates	Activates	2,002	2.60	2.23	3.06	5.44×10^{-29}	6.3×10^{-20}
Pioneered	Activates	Activates	Inhibits	2,002	1.08	0.80	1.25	9.0×10^{-01}	8.5×10^{-01}
Non-Pioneered	Activates	Independent	Activates	1,836	1.90	1.57	2.30	2.45×10^{-10}	1.0×10^{-06}
Non-Pioneered	Activates	Independent	Inhibits	1,836	1.05	0.82	1.32	6.33×10^{-01}	2.8×10^{-01}
Pioneered	Inhibits	Inhibits	Activates	864	0.68	0.33	1.251	2.9×10^{-01}	1.0×10^{-00}
Pioneered	Inhibits	Inhibits	Inhibits	864	2.33	1.61	3.28	8.08×10^{-06}	9.44×10^{-05}
Non-Pioneered	Inhibits	Independent	Activates	440	1.33	0.83	2.05	0.17	0.83
Non-Pioneered	Inhibits	Independent	Inhibits	440	1.72	1.34	2.43	0.008	0.23

OR: odds ratio, LB: lower boundary, UB: upper boundary, ALL DEGs: all differentially expressed genes (FDR < 0.05) in *TFAP2*-KO clones (two independent clones, 4 replicates each) and WT (4 replicates) SK-MEL-28 cells. Log2FC: Log base 2 fold change. N: numbers of TFAP2 regulated enhancer peaks used in the analysis.

Table 2: Hypergeometric analysis: TFAP2-activated enhancer and promoters, and TFAP2-activated gene expression

Enhancers and promoters	Effect of TFAP2 on H3K27Ac	Effect of TFAP2 on ATAC	Effect of TFAP2 on RNA-seq	N (# of elements)	OR	LB	UB	p-value Log2FC < -1
All peaks	-	-	Activates	36,948	1.66	1.40	1.98	2.4×10^{-08}
TFAP2A (open chromatin)	-	-	Activates	26,373	1.62	1.36	1.92	1.6×10^{-08}
TFAP2A peaks	Activates	-	Activates	4,601	3.11	2.57	3.9	6.0×10^{-24}
TFAP2A peaks	Activates	Independent	Activates	2,324	2.75	2.10	3.55	2.1×10^{-12}
TFAP2A peaks	-	Activates	Activates	5,443	2.58	2.3	2.89	3.9×10^{-27}
TFAP2A peaks	Independent	Activates	Activates	3,241	2.97	2.73	3.70	8.8×10^{-19}
TFAP2A peaks	Activates	Activates	Activates	2,202	4.4	3.46	5.58	4.1×10^{-27}
TFAP2A peaks	Activates OR	Activates	Activates	7,842	3.80	3.1	4.60	1.44×10^{-35}
TFAP2A peaks	Independent	Independent	Activates	19,570	1.55	1.39	1.73	6.1×10^{-02}

OR: odds ratio, LB: lower boundary, UB: upper boundary, Log2FC: Log base 2 fold change. Differentially expressed genes in *TFAP2*-KO clones (two independent clones, 4 replicates each) and WT (4 replicates) SK-MEL-28 cells. N: numbers of TFAP2 regulated enhancer and promoter peaks used in the analysis.

TFAP2A inhibits enhancers by blocking the opening of chromatin

Because of evidence that TFAP2A directly represses gene expression (Lin et al., 2016; Liu et al., 2007; Wong et al., 2012) we next sought to identify candidates for enhancers directly inhibited by TFAP2 paralogs. To this end we filtered promoter-distal TFAP2A peaks for those where the local H3K27Ac signal was higher in *TFAP2*-KO cells than in WT cells (adj. p <0.05, log2FC>1). Analogously to TFAP2-activated enhancers, candidate TFAP2-inhibited enhancers were split between a subset where the ATAC-seq signal was higher in *TFAP2*-KO cells than in WT cells (i.e., TFAP2-inhibited) (**Fig. 2C, G-G'**) and a subset where it was TFAP2-independent (**Fig. 3D, H-H'**). The first subset was significantly associated with TFAP2-inhibited genes (**Fig. 3K**, **Table 1 and Table 3**) and the average H3K4me3 signal at these sites was TFAP2-inhibited (**Fig. 3G''**). Because TFAP2 concomitantly inhibits enhancer activity and chromatin accessibility, we define these enhancers as inhibited by TFAP2 in pioneer factor-mode. The binding site for TFAP2 site was strongly enriched for in these sites, as were those for ETS1 and CTCF (**Fig. 3O**), both transcriptional repressors (Kim et al., 2015; Mavrothalassitis and Ghysdael, 2000). By contrast, the subset of candidate TFAP2-inhibited enhancers where the

ATAC-signal was TFAP2-independent was not associated with TFAP2-inhibited genes (**Fig. 3L**, **Table 1**), and the average H3K4me3 signal at them was TFAP2 independent (**Fig. 3H''**). We infer these elements are not TFAP2-inhibited enhancers, despite having elevated H3K27Ac signal in TFAP2-KO cells in comparison to WT cells. In conclusion, at TFAP2-inhibited enhancers TFAP2 recruits machinery that condenses chromatin and inhibits enhancer activity; the canonical pioneer factor FOXA1 also has this potential (Sekiya and Zaret, 2007; Watts et al., 2011).

Table 3: Hypergeometric analysis: TFAP2-inhibited enhancers and promoters, and TFAP2-inhibited gene expression

Enhancers and promoters	Effect of TFAP2 on H3K27Ac	Effect of TFAP2 on ATAC	Effect of TFAP2 on RNA-seq	N (# of elements)	OR	LB	UB	p-value |Log2FC| >1
TFAP2A (closed chromatin)	-	-	Inhibits	12,931	1.39	1.15	1.69	8.0×10^{-04}
TFAP2A (open chromatin)	-	-	Inhibits	26,373	1.06	0.90	1.25	4.8×10^{-01}
TFAP2A peaks	Inhibits	-	Inhibits	2,830	1.68	1.31	2.13	5.1×10^{-05}
TFAP2A peaks	-	Inhibits	Inhibits	4,236	1.69	1.34	2.12	1.33×10^{-05}
TFAP2A peaks	Inhibits	Inhibits	Inhibits	1,695	2.06	1.51	2.76	8.47×10^{-06}
TFAP2A peaks	Inhibits OR	Inhibits	Inhibits	5,371	1.68	1.38	2.03	3.61×10^{-07}
TFAP2A peaks	Independent	Independent	Inhibited	21,848	0.98	0.82	1.15	7.0×10^{-01}

OR: odds ratio, LB: lower boundary, UB: upper boundary, Log2FC: Log base 2 fold change. Differentially expressed genes in *TFAP2*-KO clones (two independent clones, 4 replicates each) and WT (4 replicates) SK-MEL-28 cells. N: numbers of TFAP2 regulated enhancer and promoter peaks used in the analysis.

We similarly analyzed whether and how TFAP2 directly activates or directly inhibits promoters. Although TFAP2A peaks are frequently found at promoters (8277 genes have a TFAP2A peak within 1 kb of the TSS), it was uncommon for the underlying H3K27Ac and H3K4Me3 signal to be elevated or reduced in *TFAP2* KO cells relative to in WT cells (119 and 31 candidate for directly activated and directly inhibited promoters, respectively). Similar to the trends for TFAP2-regulated enhancers, the pioneered subset of TFAP2-activated promoters was more strongly associated with TFAP2-activated genes than the non-pioneered subset, and only the pioneered subset of TFAP2-inhibited promoters was associated with TFAP2-inhibited genes (**Supplemental Fig. S6A-L; additional examples in Supplemental Fig. S7A-B**).

At additional subsets of MITF peaks overlapping TFAP2A peaks, TFAP2 facilitates chromatin access for MITF both in pioneer and non-pioneer factor modes

A prediction of the TFAP2-as-pioneer-factor model is that binding of transcription factors, like MITF, will depend on TFAP2. Among 37,643 MITF peaks in WT SK-MEL-28 cells that we previously identified by CUT&RUN (Dilshat et al., 2021), 15,752 (42%) overlap a TFAP2A peak (i.e., assessed in this study). Of these, 9,413 (60%) were within open and active chromatin (**Supplemental Fig. S8A**). To assess MITF binding in the absence of TFAP2 we carried out anti-MITF CUT&RUN in *TFAP2*-KO cell lines. Of note, as *MITF* RNA levels in *TFAP2*-KO cells are only about 60% of those in WT cells, an across the board decrease in the average height (read depth) of MITF peaks was possible. Instead, we observed that the average height of MITF peaks not overlapping TFAP2A peaks was equivalent in *TFAP2*-KO cells and in WT (**Supplemental Fig. S8B**). By contrast, among MITF peaks overlapping TFAP2A peaks (15,752), the height of 5,443 (35%) was significantly lower in *TFAP2*-KO cells than in WT cells (adj. p <0.05, log2FC < -1). (**Fig. 3A-D; Supplemental Fig. S8C-D and Supplemental Fig. S9**). We refer to these as "TFAP2-dependent MITF peaks," referring only to MITF peaks that appear to be directly TFAP2-dependent (because they overlap TFAP2A peaks in WT cells).

We reasoned that TFAP2 paralogs could facilitate MITF binding by displacing nucleosomes (i.e., in pioneer factor mode) or alternatively by elevating MITF's affinity for open DNA. Consistent with both models, we observed that TFAP2-dependent MITF peaks were in three subsets with respect to the TFAP2-dependence of the underlying ATAC-seq signal. At about 57% (3,083/5,443) the ATAC-seq signal was significantly lower (**Fig. 3B-C, 3F-F'**), at 37% (2,022/5,443) it was unchanged (**Fig. 3D, 3G-G'**), and at 6% it was higher (**Fig. 3E, 3H-H'**) in *TFAP2*-KO cells than in WT cells. The first two subsets were strongly associated with TFAP2-activated genes (Hypergeometric test; p-value = 8.4×10^{-26} and p-value = 1.07×10^{-13} respectively) and with MITF-activated genes (Hypergeometric test; p-value = 1.16×10^{-21} and p-value = 4.3×10^{-11} respectively) **(Table 4)**. We infer that at the first subset, TFAP2 is

a pioneer factor, facilitating access for MITF and other transcription factors (illustrated in **Fig. 3F''**). Supporting this prediction, the transcription factor binding sites for MITF, SOX10, RUNX and FRA1 were strong enriched at such elements (**Fig. 3F'''**). At the second subset, TFAP2 is a transcriptional activator that recruits MITF, also functioning as a transcriptional activator; we presume another protein serves as a pioneer factor at this subset (illustrated in **Fig. 3G''**). Consistent with this notion, the binding site for JUN, a widely deployed pioneer factor (Vierbuchen et al., 2017), site is strongly enriched in these elements (**Fig. 3G'''**). Examples are shown of TFAP2-dependent MITF peaks near *FRMD4B, CYP7B1, TRPM1 SOX9, EDNRB, MREG, GPR143, SNAI2, MEF2C, MYO5A, PAX3, EN1* and *FOXI3* genes (**Fig. 3B-D and Supplemental Fig. S8D**). At the third subset of TFAP2-dependent MITF peaks, where ATAC-seq signal was higher in *TFAP2*-KO cells than in WT cells (**Supplemental Fig. S10A-A'**), TFAP2 may serve as a pioneer factor for MITF in MITF's proposed role as transcriptional repressor (Dilshat et al., 2021) (**illustrated in Supplemental Fig. S10A''**). However, this category of element was not enriched near genes inhibited by either TFAP2 or MITF (Hypergeometric test; p-value = 6.02 x 10^{-02} and p-value = 9.12 x 10^{-02} respectively). These results are consistent with TFAP2 facilitating access for MITF, in its transcriptional activator form, to enhancers in both pioneer-factor and non-pioneer factor modes.

Table 4: Hypergeometric analysis: TFAP2-dependent MITF peaks and gene expression

TFAP2's effect on: MITF	Effect of TFAP2 on ATAC	Effect of TFAP2 on RNA-seq	N (# of elements)	OR	LB	UB	p-value All DEG's	p-value |Log2FC| >1
TFAP2-dependent	-	Activates	5,443	2.96	2.56	3.43	3.47×10^{-41}	8.4×10^{-26}
TFAP2-dependent	-	Inhibits	5,443	1.00	0.81	1.23	9.5×10^{-01}	7.2×10^{-01}
TFAP2-dependent	Activates	Activates	3,083	3.43	2.95	3.98	3.19×10^{-49}	1.16×10^{-26}
TFAP2-dependent	Activates	Inhibits	3,083	1.15	0.92	1.42	1.7×10^{-01}	4.0×10^{-01}
TFAP2-dependent	Independent	Activates	2,358	2.38	1.81	2.55	1.6×10^{-16}	1.07×10^{-13}
TFAP2-dependent	Independent	Inhibits	2,358	1.13	0.91	1.40	2.3×10^{-01}	4.0×10^{-01}
Mutually dependent	Activates	Activates	717	2.967	1.768	4.756	3.47×10^{-05}	9.28×10^{-05}
Mutually dependent	Activates	Inhibits	717	0.789	0.284	1.772	7.07×10^{-01}	1.00
TFAP2-inhibited	Inhibits	Activates	924	0.73	0.48	1.06	1.11×10^{-01}	1.00
TFAP2-inhibited	Inhibits	Inhibits	924	2.75	2.21	3.39	1.1×10^{-17}	3.5×10^{-04}
TFAP2-inhibited	Independent	Activates	681	1.18	0.80	1.68	1.00	1.00
TFAP2-inhibited	Independent	Inhibits	681	2.27	1.72	2.94	2.9×10^{-08}	1.2×10^{-02}

OR: odds ratio, LB: lower boundary, UB: upper boundary, ALL DEGs: all differentially expressed genes in *TFAP2*-KO clones (two independent clones, 4 replicates each) and WT (4 replicates) SK-MEL-28 cells. Log2C: Log base 2 fold change. N: numbers of TFAP2–dependent MITF peaks used in the analysis.

To test for the converse dependence, we carried out anti-TFAP2A CUT&RUN in *MITF*-KO cells. *TFAP2A* mRNA levels were equivalent in *MITF*-KO and WT cells, and the average TFAP2A peak height was globally equivalent by CUT&RUN. At 13% (717/ 5334) of TFAP2-dependent MITF peaks, the TFAP2A peak was, reciprocally, significantly reduced in *MITF*-KO cells (**Fig. 3A, C**). At such loci, the average ATAC-seq was reduced in *TFAP2*-KO cells than in WT cells (**Fig. 3C, 3I-I'**). We termed these peaks mutually-dependent (**illustrated in Fig. 3I''**). Interestingly, mutually-dependent MITF/ TFAP2 peaks were enriched in binding motifs for TFAP2, MITF, BRM2 and TEAD4 but, notably and unlike the other subsets of TFAP2-dependent MITF peaks, not for SOXE (**Fig. 3I'''**). SOX10 co-binds many loci with MITF (Laurette et al., 2015), if SOX10 is absent from mutually-dependent peaks this may explain the dependence of TFAP2 binding on MITF at these sites. At ~40% (288/ 717) of the mutually dependent peaks, the polycomb repressive histone mark H3K27Me3 was significantly higher (including in the gene body) in *MITF*-KO cells

but, unexpectedly, not in *TFAP2*-KO cells, even though MITF binding was lower in *TFAP2*-KO cells **(illustrated in Fig 3I'', Supplemental Fig. 8E-G**).

In summary, at about one third of MITF peaks that overlap TFAP2A peaks the MITF binding depends on TFAP2. Such TFAP2-dependent MITF peaks occur both at loci where nucleosome packing depends on TFAP2 (pioneer factor mode) and where it does not (non-pioneer factor mode). At a subset of TFAP2-dependent MITF peaks where TFAP2 acts in pioneer factor mode and characterized by the absence of SOXE binding site TFAP2A binding is, reciprocally, MITF-dependent.

At additional subsets of MITF peaks overlapping TFAP2A peaks, TFAP2 paralogs inhibit or have no effect on chromatin access for MITF

In Figure 2 we established that at some TFAP2A peaks, TFAP2 paralogs close chromatin, and presumably inhibit binding of transcription factors. Consistent with this prediction, among MITF peaks overlapping TFAP2A peaks, the height of 10% (1,605) was higher in *TFAP2*-KO cells than in WT cells (**Fig. 3A, E; Supplemental Fig. S9**). At 58% (924/1,605) of these, the ATAC-seq signal was also significantly higher in *TFAP2*-KO cells versus in WT cells (**violin plot**, **Fig. 3H, H', illustrated in Fig. 3H''**). A unique set of transcription factor binding sites, including that for SP1, NFY, JUN and TFE3, were enriched among such elements (**Fig. 3H'''**). Moreover, these elements were modestly associated with TFAP2-inhibited genes**.**

Of note, at the majority of MITF peaks that overlap TFAP2A peaks (65%, 10,418/ 15,752), the height was equivalent in TFAP2-KO and WT cells (**Supplemental Fig. S9**). Interestingly TFAP2-independent MITF peaks were not strongly enriched for the TFAP2 binding site (**Supplemental Fig. S11A**), implying that TFAP2 is attracted to many of these sites via other proteins rather than binding directly to the DNA. Such indirect binding may be less avid, as the average height TFAP2-independent MITF peaks was smaller than that of TFAP2-dependent MITF peaks (compare WT MITF signal in (**Supplemental Fig. S9, compare cluster 1 and 4 in WT cells**). As expected, TFAP2-independent MITF peaks were associated neither with TFAP2-activated nor TFAP2-inhibited genes.

TFAP2 and MITF co-regulate genes in the melanocyte gene regulatory network

The delayed pigmentation in zebrafish *tfap2a/tfap2e* double mutants was consistent with two mechanisms which are not exclusive of one another. In the first mechanism, TFAP2 paralogs directly activate *MITF* expression, and thereby indirectly activate expression of pigmentation genes. In the second mechanism, TFAP2 paralogs directly activate expression of pigmentation genes. Supporting the first mechanism, there is a pioneered TFAP2-activated enhancer in intron 2 of the *MITF* gene (**Supplemental Fig. S12**), and *MITF* mRNA levels are about 40% lower in TFAP2-KO cells than in WT cells. However, the first mechanism predicts that loss of TFAP2 would most strongly diminish the expression of the most highly MITF-dependent genes. However, many of the genes whose expression was most strongly reduced in *MITF*-KO cells compared to in WT cells were completely TFAP2-independent, or indeed were TFAP2-inhibited (**Supplemental Table 4**). To assess the second mechanism, we identified the set of genes activated directly by MITF, defined as MITF-activated genes associated with an MITF peak, and the set of genes directly activated by TFAP2, defined as TFAP2-activated genes associated with an TFAP2-activated enhancer (i.e., of pioneered or non-pioneered variety). Supporting the second mechanism, genes activated directly both by TFAP2 and by MITF were enriched for GO terms related to pigmentation (**Fig. 4B**), although genes related to pigmentation were among those apparently directly regulated solely by MITF or TFAP2 paralogs (**Fig. 4C**) (Baxter et al., 2019). We took a similar approach to identify genes directly inhibited by TFAP2 and/or by MITF (**Fig. 4D**). Genes directly inhibited by both were strongly enriched for GO terms related to cell adhesion and cell migration (**Fig. 4E**). In summary, reduced expression of pigmentation genes and elevated expression of invasion genes in *TFAP2*-KO cells compared to in WT cells is largely explained by the direct activation and inhibition, respectively, of these categories of genes by TFAP2 paralogs.

Considering the strong correlation of TFAP2-inhibited genes with cell migration we performed *in vitro* scratch-recovery-assays and characterized the migrative capacity of our TFAP2-KO cells. Unexpectedly, while WT SK-MEL-28 cells closed the wound after 24 hours, both of our *TFAP2*-KO clones (clone 4.3 and clone 2.12) failed to close the wound within that time (**Supplemental Fig. 13D**). This finding also contrasts with the observation that the expression *tfap2e* correlates negatively with the migratory capacity of zebrafish models of melanoma (Campbell et al., 2021), but

it is consistent with the accumulation of melanocytes in the dorsum of zebrafish *tfap2a* knockout embryos (Barrallo-Gimeno et al., 2004; Knight et al., 2004; Knight et al., 2003) and *tfap2a/ tfap2e* double mutant embryos (**Fig. 1, Supplemental Fig.S1**). Furthermore, these results are consistent our previous findings that knocking-down MITF negatively influences cell migration and invasion (Dilshat et al., 2021). The reduced migrative capacity of *TFAP2*-KO cells may be attributed to the strong up-regulation of genes associated with cell adhesion in *TFAP2*-KO cells.

Finally, we considered how TFAP2 paralogs might regulate the phenotype in melanoma cells. Advanced melanoma is characterized by lower levels of TFAP2A than benign nevi (e.g., Huang et al., 1998), and low transcript levels of *tfap2* paralogs are associated with an invasive phenotype in zebrafish melanoma (Campbell et al., 2021). We examined the association of TFAP2-activated and TFAP2-repressed genes (**Supplemental Fig. 13A-C**) with gene expression profiles from melanoma tumors and melanoma cell lines with distinct phenotypes (Hoek et al., 2008a; Hoek et al., 2006; Jonsson et al., 2010; Rambow et al., 2018; Tirosh et al., 2016; Tsoi et al., 2018; Verfaillie et al., 2015). Enrichment analysis showed (Yu et al., 2012) melanoma profiles previously found to be associated with high levels of MITF activity were enriched for genes directly activated by TFAP2, including the subset associated with TFAP2-dependent MITF peaks (**Fig. 4F**). Moreover, melanoma profiles associated with low levels of MITF activity were enriched for genes directly by TFAP2 (**Fig. 4F**).

Discussion

In this study, we confirm that Tfap2 paralogs are necessary for timely pigmentation in zebrafish embryos, as well as for normal levels of the expression of pigmentation genes in a melanoma cell line. We also describe how Tfap2 affects expression of such genes, and test the hypothesis that it makes chromatin more accessible to MITF, a transcription factor known to directly regulate the expression of pigmentation genes. The latter involved assessing the consequences of the loss of *MITF* alone, and that of both *TFAP2A* and *TFAP2C*, on global gene expression; on chromatin

marks indicative of enhancers, promoters, and repressed chromatin; on nucleosome positioning; and on the binding of TFAP2A to chromatin in *MITF* mutants and that of MITF to chromatin in *TFAP2A/TFAP2C* double mutants. Integration of these datasets yielded a deeper understanding of the mechanisms whereby TFAP2 regulates gene expression than could be acquired by more traditional methods.

Integrating genomic data sets permitted us to identify genomic elements that were bound by TFAP2A in WT cells and that either lost or gained H3K27Ac signal in TFAP2-KO cells; we inferred that these elements were enhancers directly activated or inhibited by TFAP2. Of note, only a minority of TFAP2A peaks coincided with TFAP2-dependent enhancers. As expected by the Tfap2 as pioneer factor model, at a subset of TFAP2A-dependnet enhancers the ATAC-signal was TFAP2-activated. Interestingly, there were elements where the ATAC-seq signal was TFAP2 activated but the H3K27Ac signal independent and such elements were strongly associated with TFAP2-activated genes. It was also interesting that at a subset of TFAP2-inhibited enhancers, loss of TFAP2 led to opening of the chromatin, implying that TFAP2 paralogs recruit distinct transcription factors, and that these in turn recruit either enzymes that open chromatin or enzymes that condense it, in locus-specific fashion. The latter is consistent with findings for FOXA1, which has been shown to recruit proteins that condense chromatin, like GRG3 (Sekiya and Zaret, 2007; Watts et al., 2011).

A second discovery from our analyses is that TFAP2 can activate enhancers in a non-pioneer factor mode. At a subset of TFAP2A peaks where the H3K27Ac signal was TFAP2-activated, the ATAC-seq signal was TFAP2-independent. Further evidence that such elements are TFAP2-dependent enhancers is that their average H3K4Me3 signal was also TFAP2-dependent. We infer that TFAP2 activates and inhibits these enhancers, but not as a pioneer factor. At such enhancers the continued presence of TFAP2 is necessary for continued acetylation of histone H3 lysine 27 (H3K27Ac), which fits with evidence that TFAP2 binds the histone acetyl transferase p300/CBP (Braganca et al., 2003) and inhibits the NURD histone-deacetylase complex (White et al., 2021). TFAP2 may attract other transcription factors without affecting nucleosome positioning; indeed, some TFAP2-dependent MITF peaks were found at Non-pioneered TFAP2- activated enhancers. The fact that

497 the TFAP2 binding site is not strongly enriched at these Non-pioneered TFAP2-
498 activated enhancers may imply that TFAP2 binds these elements indirectly. Finally,
499 we refer to these elements as non-pioneered TFAP2-activated enhancers because
500 in the absence of TFAP2 their activity is lost but chromatin stays open. Our
501 experimental design could not rule out the possibility that TFAP2 stably pioneered
502 these elements such that chromatin remained open (but not active) after TFAP2 was
503 removed. A precedent for this scenario is that at a subset of elements pioneered by
504 PAX7, chromatin remains open after the removal of PAX7 (Mayran et al., 2018).
505 However, the observation that TFAP2 site is less enriched compared to that of
506 pioneered TFAP2-activated enhancers, and that the binding sites of pioneer factors
507 FOS and JUN are enriched (Bejjani et al., 2019), supports the alternative model that
508 such elements are simply pioneered by different transcription factors.
509
510 A third finding from this study is that at a subset of MITF/TFAP2A co-bound peaks,
511 MITF binding was reduced in *TFAP2*-KO cells. A subset of such TFAP2-dependent
512 MITF peaks were present at Pioneered TFAP2-activated enhancers, and at *TFAP2*-
513 independent NDRs (some of which were Non-pioneered TFAP2-activated
514 enhancers, where the mechanism of recruitment of MITF is distinct). Thus, TFAP2
515 modulates MITF activity at certain loci by providing access to chromatin. Of note, at
516 a subset of MITF/TFAP2A peaks, TFAP2 binding was lost in *MITF*-KO cells. There is
517 precedent for reciprocal binding for pioneer factors, in the cases of both FOXA1 and
518 steroid hormone receptors, at subsets of sites where they are co-bound (Swinstead
519 et al., 2016a). Why are all MITF/TFAP2A peaks not mutually dependent? Notably, at
520 many MITF/TFAP2A mutually dependent peaks, the repressive mark H3K27Me3
521 accumulated in MITF-KO cells. This is consistent with evidence a) that the SWI/SNF
522 complex, which MITF probably recruits to such loci, competes for access to
523 chromatin against the Polycomb repressor complex, which deposits H3K27Me3
524 (Wilson et al., 2010), and b) that the binding of pioneer factors is impeded by
525 condensed H3K27me3-positive chromatin (Petruk et al., 2017; Wilson et al., 2010).
526 A possible explanation for this is that at TFAP2-dependent MITF peaks, some
527 measure of BRG1 binding is retained, possibly recruited by another activator like
528 SOX10, in MITF KO cells, but this is not the case for MITF/TFAP2A mutually
529 dependent peaks.
530

Finally, our results suggest a mechanism that could account for how TFAP2 promotes the pigmentation of embryonic melanophores, the expression of pigmentation genes, and possibly the proliferation of melanoma cells. First, *MITF* expression is lower in *TFAP2*-KO than WT cells. Second, because TFAP2 facilitates binding of MITF to enhancers and promoters of genes that govern pigmentation, the presence of TFAP2 leads to higher expression of those genes. Although the set of MITF-activated but TFAP2-independent genes was not enriched for pigmentation genes, it did include some such genes including *MLANA*, *TYRP1* and *PMEL.* Notably, despite lower MITF mRNA expression in *TFAP2*-KO cells, binding of MITF was unchanged at such genes. This might explain why zebrafish embryonic melanocytes become pigmented more slowly in *tfap2a/tfap2e* double mutants: the number of melanophores in these mutants animals was reduced in embryos depleted for *tfap2a*, singly or in combination with *tfap2e*, and the doubling time of TFAP2-KO cells was longer than that of their WT counterparts. Also, MITF is known to promote proliferation, but whether TFAP2 and MITF cooperate to promote proliferation remains unclear. The expression of genes promoting cell migration and invasion has been observed to be higher in cells with low versus high MITF activity (Rambow et al., 2019). Indeed we show evidence suggesting that TFAP2 paralogs directly suppress such genes, consistent with our previous findings (Campbell et al., 2021). Thus, independent of its other activities as a transcription factor, TFAP2 determines which genes can be activated by MITF. In summary, MITF activity in melanoma cells – and thus the phenotypes of these cells – depend in part on the presence of transcription factors that give MITF access to specific regulatory elements.

Materials and Methods

Zebrafish lines and maintenance

D. rerio were maintained in the University of Iowa Animal Care Facility according to a standard protocol (protocol no. 6011616). All zebrafish experiments were performed in compliance with the ethical regulations of the Institutional Animal Care and Use Committee at the University of Iowa and in compliance with NIH guidelines.

Zebrafish embryos were maintained at 28.5℃ and staged by hours or days post-fertilization (hpf or dpf).

Generation of a zebrafish *tfap2e* loss-of-function allele

To generate the tfap2e loss-of-function allele, we designed paired (e.g., left and right) zinc finger nucleases (ZFN) targeting exon 2 of the tfap2e locus resulting in non-homologous end-joining and disruption of the open reading frame for Tfap2e. Briefly, the online tool, ZiFiT (Sander et al., 2010), was used to identify an optimal ZFN target site [utilizing the CoDa approach (Sander et al., 2011). Once identified, a custom DNA fragment encoding the entire left or right zinc finger array (ZFA) along with flanking XbaI and BamHI restriction sites was synthesized (Integrated DNA Technologies, Coralville, IA). Subsequently, the ZFA fragment was subcloned into pMLM290 (Addgene, plasmid 21872), which includes a modified FokI nuclease domain (Miller et al., 2007). Next, the fully assembled ZFN was PCR amplified, directionally cloned into pENTR-D/TOPO (ThermoFisher Scientific), and finally subcloned into pCS2+DEST using Gateway LR Clonase II enzyme mix (ThermoFisher Scientific). Once assembled, the final pCS2+ plasmids were sequence verified, linearized, mRNA synthesized in vitro (mMessage mMachine SP6 Kit, Ambion/ThermoFisher Scientific). Synthesized RNA was cleaned using the Qiagen RNeasy Kit (Qiagen) and both left and right ZFN components were co-injected into 1-cell stage zebrafish embryos. Following injections, embryos were initially screened via PCR and restriction enzyme digest to confirm editing at the target site. Upon confirmation, additional embryos from a similar clutch (F0's) were allowed to develop into adulthood, 'mosaics' identified and out-crossed, and a stable F1 generation isolated.

Cell lines, reagents, and antibodies

The cells referred to as WT throughout the document are the parent SK-MEL-28 (HTB-72) line. They and the derivative line, delta6-MITF knockout cells (referred to as MITF-KO cells in this work), were obtained from the laboratory of Dr. Eirikur Steingrimsson. The cells were grown in RPMI 1640 medium (Gibco #5240025)

598 supplemented with 10% FBS (Gibco #10270106) at 5% CO_2 and 37°C. Cells were
599 tested for, and determined to be free of, mycoplasma. SK-MEL-28 cells harbor the
600 $BRAF^{V600E}$ and $p53^{L145R}$ mutations (Leroy et al., 2014). The following primary
601 antibodies and their respective dilutions were used in western blotting (WB) and
602 CUT&RUN experiments: anti-Tubulin (Sigma, #T6199), 1:5000 (WB); anti-MITF
603 (Sigma, #HPA003259), 1:2000 (WB), 1:100 (CUT&RUN); anti-TFAP2A (Abcam,
604 ab108311), 1:5000 (WB), 1:200 (CUT&RUN); anti-TFAP2C (Santa-Cruz #SC-12762
605 X), 1:1000 (WB); anti-H3K27Ac (EMD Millipore, #07-360), 1:100 (CUT&RUN); anti-
606 H3K4Me3 (EMD Millipore, #05-745R), 1:100 (CUT&RUN); H3K27Me3 (EMD
607 Millipore, #07-449), 1:100 (CUT&RUN); Rabbit IgG (EMD Millipore,#12-370), 1:100
608 (CUT&RUN); Mouse IgG (EMD Millipore, #12-371), 1:100 (CUT&RUN). The
609 following secondary antibodies and their respective dilutions were used: Anti-mouse
610 IgG(H+L) DyLight 800 conjugate (Cell Signaling Technologies, #5257), 1:20000; and
611 anti-rabbit IgG(H+L) DyLight 680 conjugate Cell Signaling Technologies, #5366),
612 1:100. Images were captured using an Odyssey CLx Imager (LICOR Biosciences).
613
614
615 **Purification of pA/G-MNase**
616
617 *E.coli* strain BL21-DE3 was transformed with plasmid DNA pAG-MNase-6xHis
618 (Addgene, plasmid #123461). Recombinant pAG-MNase was purified from cells
619 grown in LB medium to OD600 0.6 at 37°C. Cells were induced with 0.5 mM IPTG
620 and cultured for 16 hours at 20°C. Cell pellets were homogenized in lysis buffer (10
621 mM Tris, pH 7.5, 300 mM NaCl, 10 mM imidazole) containing lysozyme and
622 protease inhibitors, then sonicated and the slurry was cleared by centrifugation (35K
623 RPM, Ti70 rotor). The supernatant was subjected to IMAC chromatography (NI-NTA
624 column) and to size-exclusion fractionation (Superdex 75) using a BioLogic DuoFlow
625 QuadTec FPLC system (Bio-Rad). The purified pAG-MNase was concentrated by
626 buffer exchange with ultrafiltration (Amicon Ultra-15, 10K). Finally, the purified pAG-
627 MNase was diluted in dilution buffer (10 mM Tris pH7.5, 120 mM NaCl, 0.01mM
628 EDTA, and 50% glycerol), and stored at -80°C.
629
630 **Generation of *TFAP2A*; *TFAP2C* knockout cell lines (*TFAP2*-KO)**
631

TFAP2-KO clones were generated using the Alt-R CRISPR-Cas9 technology from Integrated DNA Technologies (IDT). Briefly, crRNAs targeting exon 2 of *TFAP2A* and *TFAP2C* were designed using the Cas9 guide RNA design checker tool (crRNA sequences below). Equimolar concentrations of crRNA and tracrRNA (IDT, #1072532) were annealed to form gRNA complexes. The ribonucleoprotein (RNP) complex was prepared by mixing gRNAs and Cas9 protein (IDT #1081058). SK-MEL-28 cells were transfected with constructs encoding components of RNP complexes using the Lipofectamine CRISPRmax Cas9 transfection reagent (ThermoFisher #CMAX00015) following the manufacturer's protocol. Single-cell colonies were screened by PCR and Sanger sequencing using primers flanking the cut sites (primer sequences below). Mutant clones (clone 2.12 and clone 4.3) were selected and further screened by western blotting, using anti-TFAP2A and anti-TFAP2C antibodies. The control cell lines used in this study were generated following this protocol but without adding gRNA duplexes.

crRNA	**Sequence (5'-3')**
TFAP2A_ex2_gRNA1	CGTCACGACGGCACCAGCAAGTTTTAGAGCTATGCT
TFAP2A_ex2_gRNA2	CTTACCTCACGCCATCGAGGGTTTTAGAGCTATGCT
TFAP2C_ex2_gRNA1	CGCCACGACGGGAGCAGCAAGTTTTAGAGCTATGCT
TFAP2C_ex2_gRNA2	CCACGACATGCCTCACCAGAGTTTTAGAGCTATGCT
Primers	**Sequence (5'-3')**
TFAP2A_geno_Fw	TCTCTTGTGCCCCCTCCATA
TFAP2A_geno_Rv	GCCCACCGACTGTATGTTCCA
TFAP2C_geno_Fw	CCGTGACCCCGATTTTGGAT
TFAP2C_geno_Rv	CGGCTTCACAGACATAGGCA

SDS-PAGE and Western blotting

TFAP2-KO and WT cells were washed in ice-cold PBS. RIPA buffer containing protease inhibitors (Roche, cOmplete Mini) was added and cells were lysed on ice for 20 minutes. Cell lysates were centrifuged at 14,000 g for 20 minutes and the quantity of protein in the supernatants was quantified using Bradford assays (Bio-

Rad #5000002). Laemmli sample buffer (Bio-Rad #1610747, 5% 2-mercaptoethanol) was added to 20 µg protein and samples were boiled at 95°C for 5 minutes before being loaded onto a 10% SDS-polyacrylamide gel (Bio-Rad #4568034). Protein was transferred to polyvinylidene fluoride (PVDF) membranes (Thermo Scientific #88520), which were incubated overnight with primary antibody. Membranes were washed 3 times with TBS-T and incubated with horseradish peroxidase-conjugated anti-rabbit or anti-mouse for 1 hour at room temperature, washed, and imaged using an Amersham Imager 600.

ATAC-seq

ATAC-seq was performed according to (Buenrostro et al., 2015; Liu et al., 2020) with minor alterations. Briefly, 70,000 *TFAP2*-KO cells (clone 2.12 and clone 4.3, four replicates each) and WT cells (four replicates) were lysed in ice-cold lysis buffer (10 mM Tris-HCl, pH 7.4, 10 mM NaCl, 3 mM MgCl2, 0.1% NP-40: Sigma). Transposition was performed directly on nuclei using 25 µl tagmentation reaction mix (Tagment DNA Buffer #15027866, Tagment DNA Enzyme #15027865 from Illumina Tagment DNA kit #20034210). Tagged DNA was subjected to PCR amplification and library indexing, using the NEBNext High-Fidelity 2x PCR Master Mix (New England Biolabs #M0451S) with Nextera DNA CD Indexes (Illumina #20015882), according to the following program: 72℃ for 5 minutes; 98℃ for 30 seconds; 12 cycles of 98℃ for 10 seconds, 63℃ for 30 seconds, and 72℃ for 1 minute. The PCR product was purified with 1.8 times the volume of Ampure XP beads (Beckman Coulter #A63881). Library quality was assessed using a BioAnalyzer 2100 High Sensitivity DNA Chip (Agilent Technologies). All DNA libraries that exhibited a nucleosome pattern were pooled and processed for 150bp paired-end sequencing.

ATAC-seq peak calling and differential analysis

ATAC-seq was performed using 150 bp paired-end sequencing reads. Raw ATAC-seq reads were trimmed using Trim Galore Version 0.6.3 (Developed by Felix Krueger at the Babraham Institute) and aligned to human genome assembly hg19 (GRCh37) using Bowtie 2 (Langmead and Salzberg, 2012; Langmead et al., 2009) with default parameters. Sorting, removal of PCR duplicates, and identification of fragments shorter than 100 bp as the nucleosome-depleted-regions (NDRs), was performed using BAM filter version 0.5.9. DeepTools version 3.3.0 (Ramírez et al., 2016) was used to check the reproducibility of the biological replicates and generate bigWig coverage files for visualization. Peaks were called using model-based analysis of ChIP-seq 2 (MACS2, version 2.1.1.20160309.6) (Zhang et al., 2008). NDRs for which accessibility differed between *TFAP2*-KO and WT cells were identified using DiffBind version 2.10 (Ross-Innes et al., 2012) with log2 fold-change threshold of >1 and a false discovery rate (FDR) < 0.05. NDRs that are directly regulated by TFAP2 were identified by overlapping differentially accessible NDRs with anti-TFAP2A CUT&RUN peaks; a 1-bp window was used to define overlap. Peaks were assigned to genes using GREAT with a peak-to-gene association rule of the nearest-gene-within-100 kb (McLean et al., 2010). Both the raw ATAC-seq files and processed sequencing data presented in this manuscript have been deposited in the Gene Expression Omnibus (GEO) repository (GSE number pending).

CUT&RUN

CUT&RUN sequencing was performed in *TFAP2*-KO cells (clone 2.12 and clone 4.3, two replicates each) and WT cells (two replicates) as previously described (Meers et al., 2019; Skene and Henikoff, 2017), but with minor modifications. Cells in log-phase culture (approximately 80% confluent) were harvested by cell scraping, centrifuged at 600 g (Eppendorf, centrifuge 5424) and washed twice in calcium-free wash-buffer (20 mM HEPES, pH7.5, 150 mM NaCl, 0.5 mM spermidine, and protease inhibitor cocktail cOmplete Mini, EDTA-free from Roche). Pre-activated concanavalin A-coated magnetic beads (Bangs Laboratories, Inc) were added to cell suspensions ($2x10^5$ cells) and incubated for 15 minutes at 4ºC. Antibody buffer (wash-buffer with 2mM EDTA and 0.05% digitonin) containing anti-TFAP2A, anti-MITF, anti-H3K4Me3, anti-H3K27Me3, anti-H3K27Ac or Rabbit IgG was added and

cells were incubated overnight at 4ºC. Cells were washed in dig-wash buffer (wash buffer containing 0.03% digitonin), and pAG-MNase was added at a concentration of 500 µg/mL. The pAG-MNase reactions were quenched with 2X Stop Buffer (340mM NaCl, 20mM EDTA, 4mM EGTA, 0.05% digitonin, 100 µg/mL RNAse A (10 mg/mL, Thermo Fisher Scientific #EN0531), 50 µg/mL glycogen (20mg/mL, Thermo Fisher Scientific #R0561) and 2 pg/mL sonicated yeast spike-in control). Released DNA fragments were treated with 1µL/mL phosphatase K (20mg/mL, Thermo Fisher Scientific #25530049) for 1 hour at 50ºC and purified by phenol/chloroform-extraction and ethanol-precipitation. Fragment sizes were analyzed using a 2100 Bioanalyzer (Agilent).

CUT&RUN library preparation and data analysis

CUT&RUN libraries were prepared using the KAPA Hyper Prep Kit (Roche). Quality control post-library amplification consisted of fragment analysis using the 2100 Bioanalyzer (Agilent). Libraries were pooled, brought to equimolar concentrations, and sequenced with 150 bp paired-end reads on an Illumina HiSeq X platform (Novogene, Sacramento, CA). For quality control, paired-end FASTQ files were processed using FastQC (Babraham Bioinformatics). Reads were trimmed using Trim Galore Version 0.6.3 (Developed by Felix Krueger at the Babraham Institute) and then mapped against the hg19 genome assembly using Bowtie2 version 2.1.0 (Langmead and Salzberg, 2012; Langmead et al., 2009). The mapping parameters and peak calling of MACS2 peaks (Zhang et al., 2008) were performed as previously described (Meers et al., 2019; Skene and Henikoff, 2017) against their matching control IgG samples. Differential analysis of H3K27Ac and of H3K27Me3 signal in WT and *TFAP2*-KO cells was preformed using MACS2 with a Log2 fold-change threshold of 1, and p-value < 1 x 10^{-5}. Differential H3K4Me3, MITF and TFAP2A signal in WT, *TFAP2*-KO and when mentioned *MITF*-KO cells was determined using DiffBind version 2.10.0 (Ross-Innes et al., 2012) with a Log2 fold-change threshold of 1, and FDR < 0.05. DeepTools version 3.3.0 was used to check the reproducibility of the biological replicates, to generate bigwig normalized (RPKM) coverage files for visualization and to plot average CUT&RUN-seq and ATAC-seq profiles (-plotProfile) and generate heatmaps (-plotHeatmap) of normalized reads (Ramírez et al., 2016). MultiBigwigSummary was used to extract read counts (-outRawCounts) (Ramírez et

al., 2016) and Prism was used to generate Violin and Box plots. Peaks were assigned to genes using GREAT with a peak-to-gene association rule of the nearest-gene-within-100 kb (McLean et al., 2010)

RNA-seq

Four replicate RNA-seq experiments were performed on *TFAP2*-KO cells (clone 2.12 and clone 4.3) and WT cells. Total RNA was extracted by direct cell lysis using the RNeasy Plus Mini Kit with QiaShredder (Qiagen #47134). RNA samples with an RNA integrity number (RIN) above nine were used for library generation and 150 bp paired-end sequencing on the Illumina HiSeq2500 platform (Novogene, Sacramento, CA). FASTQ sequence files were processed using FastQC (Babraham Bioinformatics) for quality control, and reads were trimmed using Trim Galore Version 0.6.3 (Developed by Felix Krueger at the Babraham Institute) and subsequently aligned to human genome assembly hg19 (GRCh37) using STAR (Dobin et al., 2013). The output of the --quantMode GeneCounts function of STAR was used for the calculation of differential transcript expression using DESeq2 (Love et al., 2014).The rlog function was used to generate log2-transformed normalized counts. Adjusted p-value < 0.05 was used as the threshold for statistically significant differences. Functional enrichment analyses was performed using PANTHER (Mi et al., 2021). A full list of genes differentially expressed between *TFAP2*-KO and WT cells is provided in Supplemental Table 1-3.

Motif analyses

Both de novo and known motifs were identified within 200 bp of TFAP2-activated and TFAP2-inhibited enhancer and promoter peak summits using HOMER (-findMotifsGenome).

Statistical analysis

Fisher's Exact Test was used to assess TFAP2-regulated elements (enhancers and promoters) with TFAP2-regulated gene expression. Data processing and analysis was performed in R and the code can be found at https://GitHub.com/ahelv/Differential_Expression. GraphPad-Prism was used to perform Students t-test as indicated in the figure legends

Wound scratch assay

A total of 500K cells were seeded per well of 6-well plate (Thermo Scientific, # 1483210) to reach confluent monolayer. Cells were incubated in serum free media for 6 hours before wounding with a 200 µL pipette tip. Scratches were manually imaged on an inverted light microscope (Leica #10445930) every 6 hours over a 24-hour time period. The distance of scratch closure between WT and *TFAP2*-KO cells were analyzed with Image J software.

Acknowledgements

This work was supported by grants from the National Institutes of Health (NIH) to RAC (R01-AR062457), and a postdoctoral fellowship from the American Association for Anatomy (CK). The ES laboratory is supported by grants 207067 and 217768 from the Research Fund of Iceland.

Author Contributions

Conceptualization: CK, RAC.
Formal analysis: CK, RD.
Funding acquisition: CK, ES, RAC.
Investigation: CK, RAC.
Methodology: CK, RD, HS, EVO, AH, GB.
Statistical analysis: CK, AH.
Supervision: ES, RAC.
Writing – original draft: CK, RAC.

Fig 1

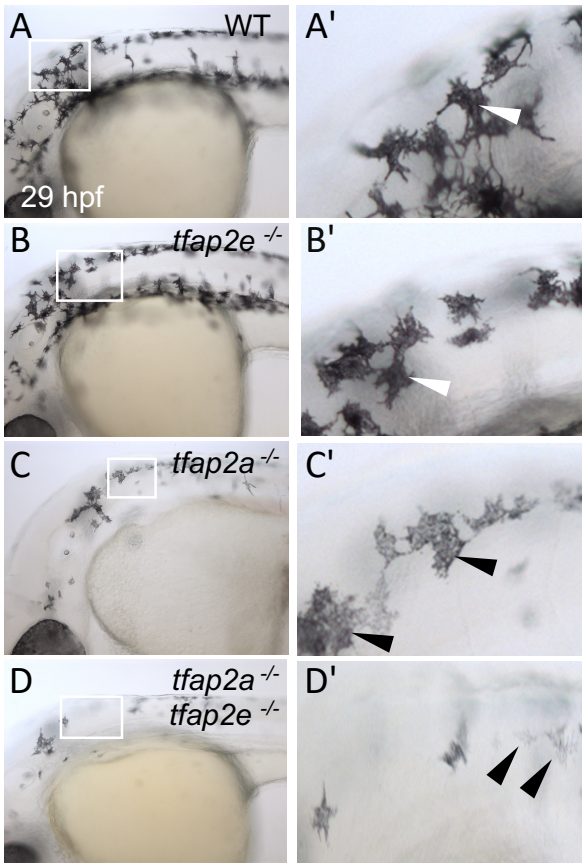

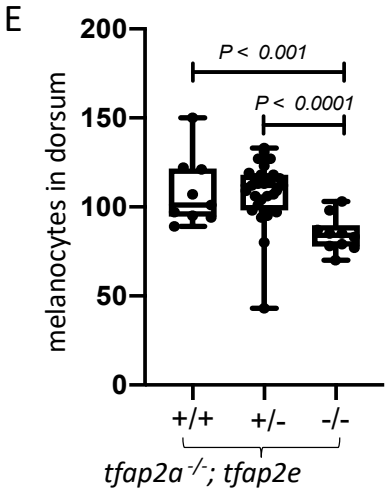

821

822

823

Fig. 2

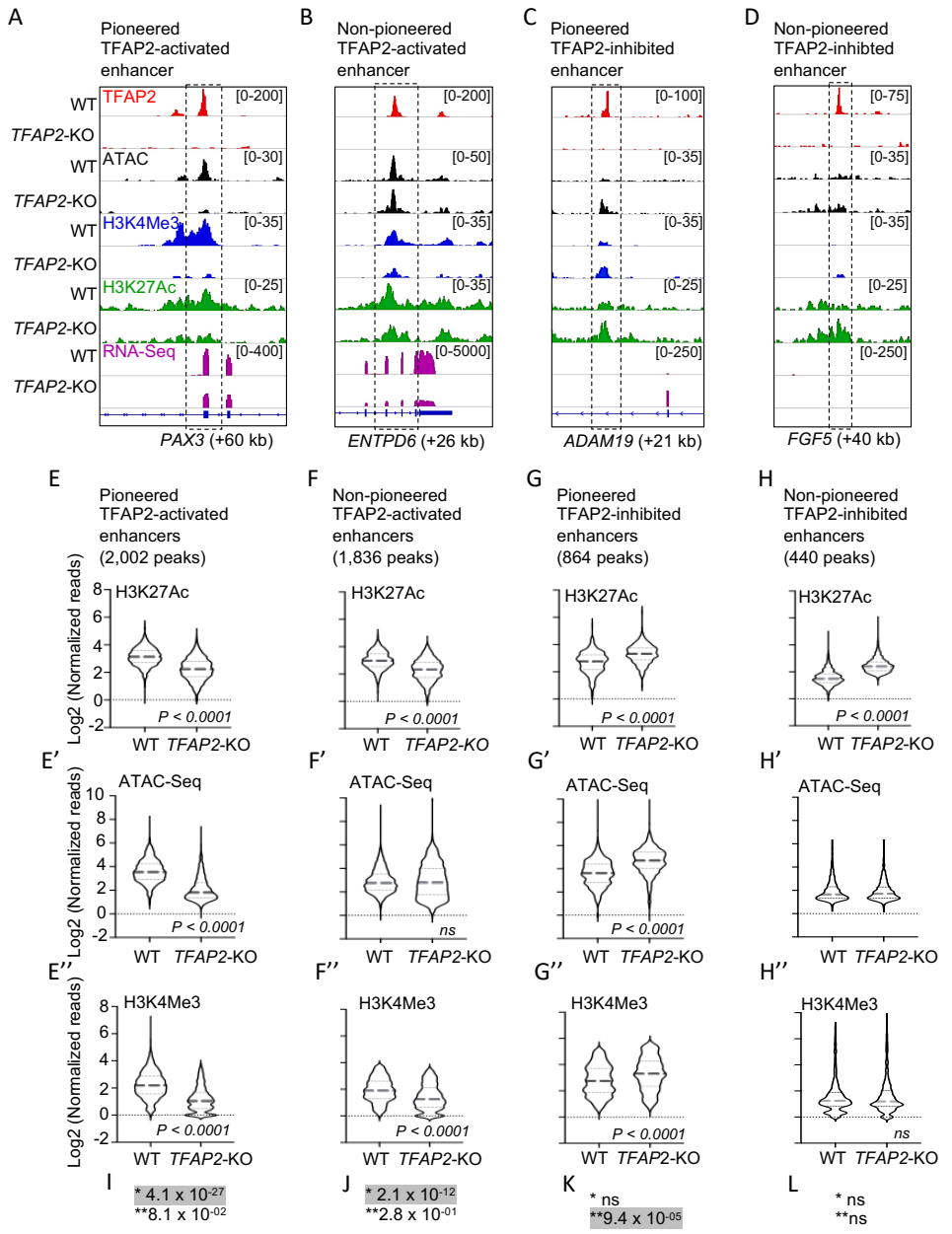

M

Pioneered TFAP2-activated enhancers

Motif	TF	Rank	P-value
	TFAP2	1,2	1 x 10-600
	EBF	3	1 x 10-51
	SOXE	4,6	1 x 10-36
	RUNX	7	1 x 10-31
	MITF	28	1 x 10-12

N

Non-pioneered TFAP2-activated enhancers

Motif	TF	Rank	P-value
	TFAP2	1	1 x 10-280
	FRA1	2	1 x 10-46
	RUNX	4	1 x 10-27
	TEAD	6	1 x 10-24
	ZFX	7	1 x 10-22

O

Pioneered TFAP2-inhibited enhancers

Motif	TF	Rank	P-value
	TFAP2	1,2	1 x 10-63
	RUNX	3	1 x 10-37
	CST6	4	1 x 10-21
	ETS1	6	1 x 10-14
	CTCF	12	1 x 10-12

Fig. 3

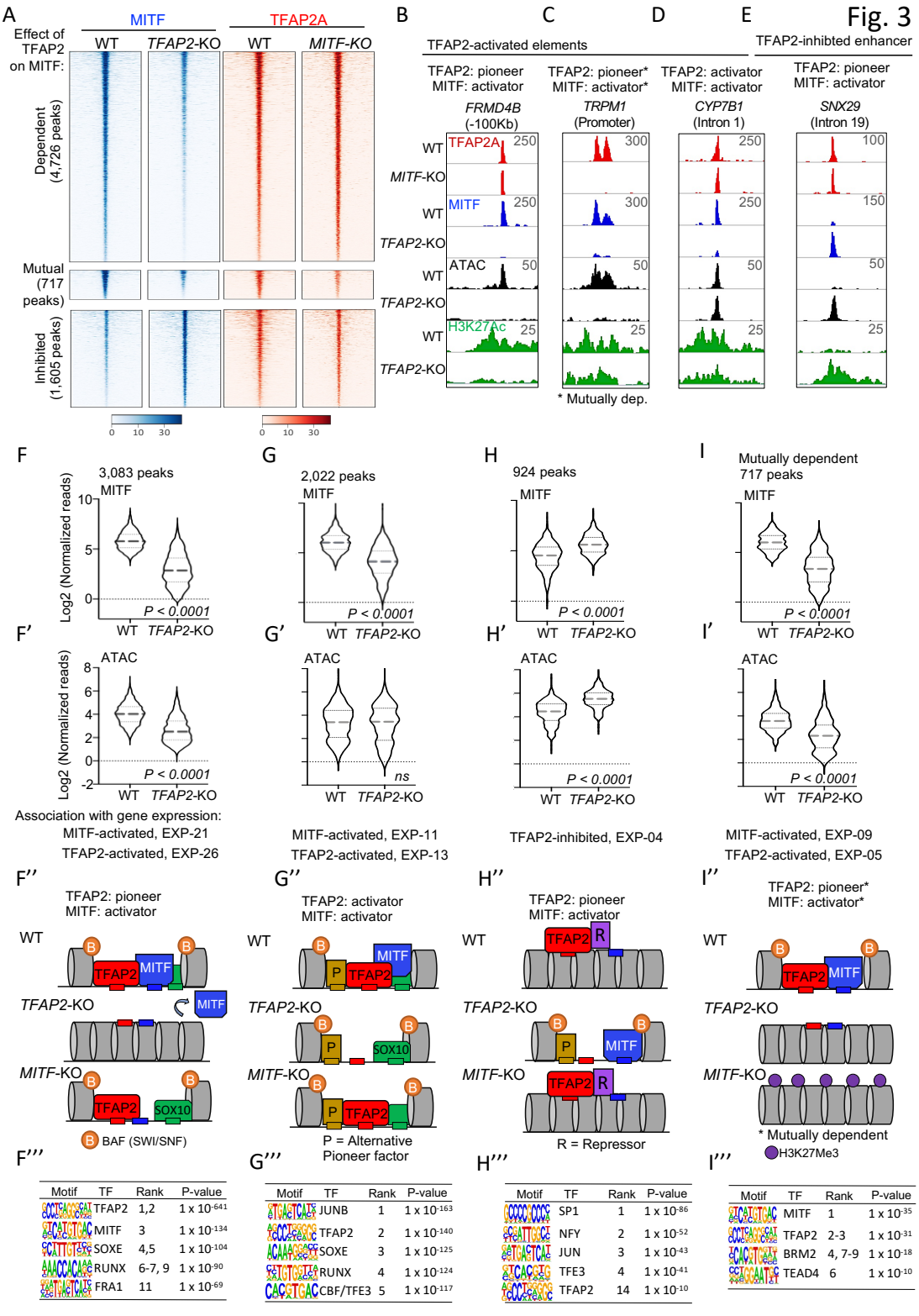

Fig. 4

A

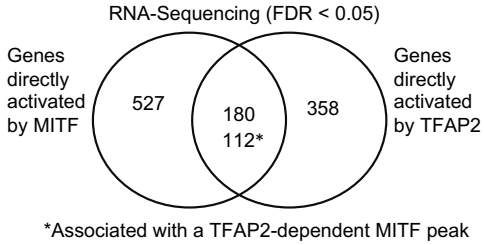

*Associated with a TFAP2-dependent MITF peak

D

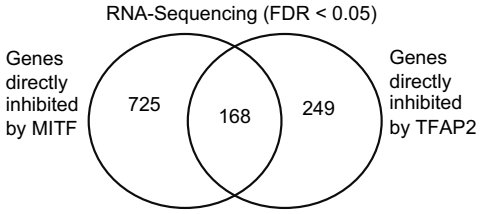

B

MITF and TFAP2-activated genes (Top 5 hits)

GO biological process	Enrichment	No. of genes	FDR
Pigmentation	16.75	11	2.79 x10^{-06}
Pigment differentiation	28.02	6	9.79 x10^{-04}
Cell differentiation	44	77	8.7 x10^{-03}
Cellular pigmentation	13.49	5	4.68 x10^{-02}
Receptor signaling	3.51	15	3.78 x10^{-02}

E

MITF and TFAP2-inhibited genes (Top 5 hits)

GO biological process	Enrichment	No. of genes	FDR
Vasculature development	6.8	32	1.8 x10^{-12}
Tube development	5.13	36	1.4 x10^{-10}
Cell motility	4.81	34	2.2 x10^{-08}
Cell migration	3.51	31	3.7 x10^{-07}
Cell adhesion	3.5	20	7.0 x10^{-06}

C

Pigmentation related genes directly activated by:

MITF	**MITF and TFAP2**	**TFAP2**
DKC1	*RAB1A*	*IGFBP7*
MLANA	*RAB32*	*KCTD15*
EIF3B	*HPS3*	*ABCA12*
KBTBD8	*CLCN7*	*CHD7*
RAB27A	*CTNNB1*	*EDNRB*
STX3	*CTSD*	*EN1*
AFG3L2	*DCT*	*HIPK2*
BNC2	*ETS1*	*HTRA1*
CCT2	*GPR143*	*MCM4*
DTNBP1	*MAFB*	*MYO5A*
IRF4	*MFSD12*	*PARN*
MLPH	*MITF*	*PAX3*
MYO10	*MREG*	*RAD21*
OSTM1	*NR4A3*	*SDC2*
PARD3	*OCA2*	*SLC2A11*
PMEL	*PEPD*	*SOX9*
PPARGC1A	*RAB38*	*SYTL2*
PSEN2	*SH3BP4*	*TFAP2C*
RPS14	*SH3PXD2A*	*ALCAM*
RPS7	*SNAI2*	*BLM*
SCUBE2	*TRPM1*	*DISC1*
SLC45A2	*VDR*	*ERBB3*
STXBP1		*FANCC*
SZT2		*LYST*
TYRP1		*MIB1*
USF2		*NBN*
VPS18		*PMCH*
		PRKDC
		SOX5

F

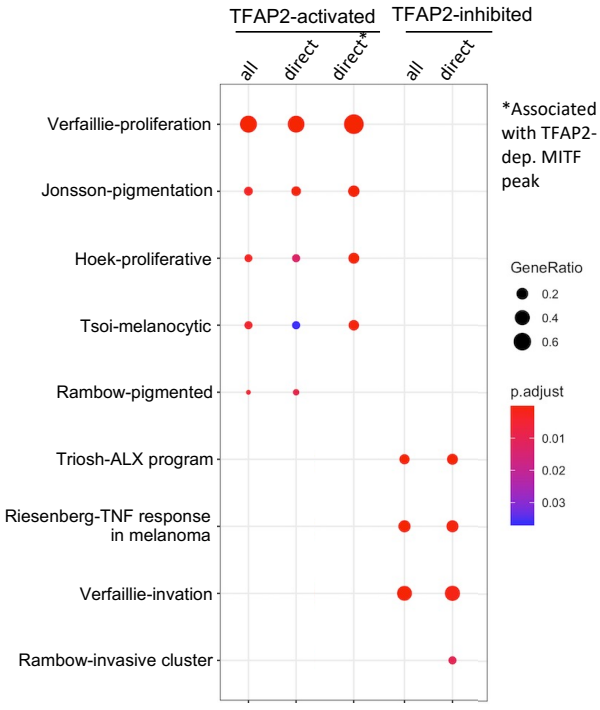

Figure legends

Figure 1: Stable KO of *tfap2e* has no effect on pigmentation in WT embryos but alters melanocyte development and delays melanin synthesis in *tfap2a* mutants. (A-D) Lateral views of head and trunk of live embryos at 29 hpf, anterior to the left and dorsal to the top. **(A-A')** A WT (sibling) embryo with normal melanocytes (white arrowhead). **(B-B')** A *tfap2e*$^{ui157ui/157}$ embryo, with melanocytes that are normal in terms of number, differentiation and pigmentation (white arrowhead). **(C-C')** A *tfap2a*$^{low/low}$ homozygous mutant embryo, with fewer melanocytes than its *tfap2e*$^{157/157}$ and WT sibling embryos. **(D-D')** A *tfap2a*$^{low/low}$*; tfap2e*$^{157/157}$ double-mutant embryo, with fewer melanin-producing melanophores than its *tfap2a*$^{low/low}$ sibling. **(E)** Box plot illustrating the number of pigmented melanocytes in the dorsum of WT (+/+), *tfap2a* mutant, *tfap2e* mutant, and double *tfap2a; tfpa2e* mutant embryos at 36 hpf. Center line, mean; box limits, upper and lower quartiles; whiskers, minimum and maximum values; black dots, number of melanocytes per individual embryo (WT; n=9, *tfap2a*$^{low/low}$*;tfap2e*$^{+/157}$, n=32; *tfap2a*$^{low/low}$*;tfap2e*$^{157/157}$, n=10). P-value according to the Student's t-test.

Figure 2: TFAP2 paralogs facilitate gene expression by opening and condensing chromatin. (A-D) Screenshot of IGV genome browser (GRCH37/hg19), visualizing anti-TFAP2A CUT&RUN-seq (red), ATAC-seq (black), anti-H3K4Me3 CUT&RUN-seq (blue), anti-H3K27Ac CUT&RUN-seq (green) and RNA-seq (magenta) datasets at **(A)** a pioneered TFAP2-activated enhancer at the *PAX3* (+60 kb) locus **(B)** a non-pioneered TFAP2A-activated enhancer at the *ENTPD6* (+26kb) locus **(C)** a pioneered TFAP2-inhibited enhancer at the *ADAM19* (+21 kb) locus and **(D)** a non-pioneered TFAP2A-inhibited enhancer at the *FGF5* (+40kb) locus. Genotypes as labeled; y-axes are grouped scaled per dataset. **(E-E'')** Violin plots representing **(E)** anti-H3K27Ac (two independent replicates) **(E')** ATAC-seq (four independent replicates) and **(E'')** anti-H3K4Me3 (two independent replicates) normalized reads at pioneered TFAP2-activated enhancers. **(F-F'')** Violin plots representing **(F)** anti-H3K27Ac **(F')** ATAC-seq and **(E'')** anti-H3K4Me3 normalized reads at non-pioneered TFAP2-activated enhancers. **(G-G'')** Violin plots

representing **(G)** anti-H3K27Ac **(G')** ATAC-seq and **(G'')** anti-H3K4Me3 normalized reads at pioneered TFAP2-inhibited enhancers. **(H-H'')** Violin plots representing **(H)** anti-H3K27Ac **(H')** ATAC-seq and **(H'')** anti-H3K4Me3 normalized reads at non-pioneered TFAP2-inhibited enhancers. P-values shown were determined by Students t-test. **(I-L)** Hypergeometric analysis of TFAP2 regulated enhancers at TFAP2-activated (*) and TFAP2-inhibited (**) genes in *TFAP2*-KO cells (FDR < 0.05, |log2FC| > 1). **(M-O)** Enrichment of transcription factor motifs at (M) pioneered TFAP2-activated enhancers, at (N) non-pioneered TFAP2-activated enhancers and at (O) pioneered TFAP2-inhibited enhancers as determined using HOMER motif analysis. P values were calculated using ZOOPS scoring (zero or one occurrence per sequence) coupled with hypergeometric enrichment analysis. TF; transcription factor.

Figure 3: TFAP2 paralogs facilitate chromatin access by MITF. (A) Density heatmaps of anti-MITF CUT&RUN-seq in SK-MEL-28 and *TFAP2*-KO cells, and anti-TFAP2 CUT&RUN-seq in SK-MEL-28 and *MITF*-KO cells at TFAP2-dependent MITF peaks (top), mutually dependent peaks (center) and TFAP2-inhibited MITF peaks (bottom). Number of peaks in each group as labelled. Regions shown are +/- 3 kb from peak center, normalized reads (RPKM). **(B-E)** Screenshot of IGV genome browser (GRCH37/hg19), showing anti-TFAP2A (red) CUT&RUN-seq in SK-MEL-28 and *MITF*-KO cells, and anti-MITF (blue) CUT&RUN-seq, ATAC-seq (black) and anti-H3K27Ac (green) CUT&RUN-seq profiles in SK-MEL-28 and *TFAP2*-KO cells. Examples of MITF binding at **(B-D)** TFAP2-activated and **(E)** TFAP2-inhibted regulatory elements. Genotypes as labeled; y-axes are grouped scaled per dataset. **(F-F')** Violin plot representing **(F)** anti-MITF CUT&RUN-seq (two independent replicates) and **(F')** ATAC-seq (four independent replicates) at 3,083 pioneered TFAP2-activated MITF peaks. **(G-G')** Violin plot representing **(G)** anti-MITF CUT&RUN-seq and **(G')** ATAC-seq at 2,022 non-pioneered TFAP2-activated MITF peaks. **(H-H')** Violin plot representing **(H)** anti-MITF CUT&RUN-seq and **(H')** ATAC-seq at 924 pioneered TFAP2-inhibited MITF peaks and **(I-I')** Violin plot representing **(I)** anti-MITF CUT&RUN-seq and **(I')** ATAC-seq at 717 mutually dependent peaks. P-value according to Students t-test, ns; not statistically significant, normalized reads RPKM. Association with gene expression; hypergeometric analysis of TFAP2-depednent and TFAP2-inhibited MITF peaks are shown at TFAP2-activated and

MITF-activated genes (FDR < 0.05, log2FC > |1|). **(F''- I'')** Schematic representation of TFAP2-dependent and TFAP2-inhibited MITF peaks as labelled; B; BAF complex (SWI/SNF), P; alternative pioneer factor. R; repressor protein. Transcription factor binding sites indicated by small rectangles, TFAP2 (red), MITF (blue) and alternative pioneer factor (yellow), example activator SOX10 (green) . **(F''' – I''')** Enrichment of transcription factor motifs using HOMER at (F''') pioneered TFAP2-dependent MITF peaks, (G''') non-pioneered TFAP2-dependent MITF peaks, (H''') TFAP2-inhibited MITF peaks and **(I''')** mutually dependent peaks. P values were calculated using ZOOPS scoring (zero or one occurrence per sequence) coupled with hypergeometric enrichment analysis. TF; transcription factor.

Figure 4: TFAP2 and MITF co-regulate pigmentation and cell differentiation genes in SK-MEL-28 cell lines. (A) Venn diagram representing directly MITF activated genes (MITF peaks within 100Kb of a TSS), based on RNA-seq, in *MITF*-KO verses WT cells (FDR < 0.05) and genes directly activated by TFAP2 (TFAP2-activated enhancers within 100Kb of a TSS), based on RNA-seq, with TFAP2-activated enhancers, in *TFAP2*-KO verses WT cells (FDR < 0.05). The number of overlapping genes with TFAP2-dependent MITF peaks are also shown (*). **(B)** Gene ontology (GO) biological process analysis (Top 5 hits) that are enriched among MITF- and TFAP2-activated genes. **(C)** A curated list of pigment-associated genes (Baxter et al., 2009) was intersected with directly MITF-activated, directly MITF/TFAP2-activated, and TFAP2-acitvated genes and represented by gene list. **(D)** Venn diagram representing directly MITF inhibited genes, based on RNA-seq, in *MITF*-KO verses WT cells (FDR < 0.05) and genes directly inhibited by TFAP2, based on RNA-seq, with TFAP2-inhibited enhancers, in *TFAP2*-KO verses WT cells (FDR < 0.05). **(E)** Gene ontology (GO) biological process analysis (Top 5 hits) that are enriched among MITF- and TFAP2-inhibited genes. GO analysis was performed using PANTHER. **(F)** Dot plot of enrichment analysis showing the enrichment of gene signatures from the literature in directly TFAP2-activated and TFAP2-inhibted genes, based on RNA-seq, in *TFAP2*-KO and SK-MEL-28 cells. P value is red lowest to blue highest; gene ratio is the ratio between genes and all genes in the GO category. Analysis of directly TFAP2-activated genes associated with TFAP2-dependent MITF peaks are shown (*).

Figure S1: *tfap2e* mutant zebrafish do not display a melanocyte phenotype whereas *tfap2a/e* double mutant zebrafish display a significant reduction in melanocyte number. **(A)** A 157 base pair mutation at the end of tfap2e exon 2 disrupts splicing and results in a premature stop codon. **(B)** PCR using primers in tfap2e exon 2 and intron 2 (e2-i2) amplifies a band of the expected 450 base pair size in tfap2e mutants but not wildtype (WT), whereas primers in exon 2 and exon 3 (e2-e3) amplify only in wildtype. NTC: not template control. **(C)** qRT-PCR analysis of tfap2e expression shows that the transcript is strongly decreased in *tfap2e*-/- mutants, consistent with nonsense-mediated decay (Student's t-test, **** p<0.0001). **(D-E)** tfap2e mutant zebrafish at 36 hpf, *tfap2e*+/- **(D)** and *tfap2e*-/- **(E)** are phenotypically indistinguishable. **(F)** Histogram illustrating the number of pigmented melanocytes in the dorsum of *tfap2e*+/- and *tfap2e*-/- mutant zebrafish embryos, **(G-H)** Zebrafish embryos from a *tfap2a*+/-;*tfap2e*+/- incross at 48 hpf. **(G)** A wildtype embryo shows normal melanocyte patterning. **(H)** A tfap2a-/- mutant embryo has fewer and paler embryonic melanocytes than wildtype**. (I)** tfap2a-/-;tfap2e+/- and (J) tfap2a-/- ;tfap2e-/- appear phenotypically indistinguishable from tfap2a-/- at 48 hpf.

Figure S2: TFAP2 binds to open and closed chromatin. (A) Screenshot of IGV genome browser (GRCH37/hg19), visualizing anti-TFAP2A and IgG CUT&RUN-seq profiles. Peaks were called using MACS2 software (two independent replicates) and are illustrated by blue bars under the anti-TFAP2A track. **(B)** Density heatmap centred on the 36,867 TFAP2A peaks identified by anti-TFAP2A CUT&RUN in WT SK-MEL-28 cells. Regions shown are +/- 3 kb from peak center, Peaks were grouped by distance to an annotated transcriptional start site. Promoter peaks +/- 3kb from a TSS and enhancers >3 kb from an TSS. Anti-TFAP2A, anti-H3K4Me3 and anti-H3K27Ac CUT&RUN-seq, and ATAC-Seq profiles are shown. Normalized reads (RPKM). **(C)** Histogram representing H3K27Ac signal, binned from low-high read-depth on the x-axis and percentage of TFAP2A promoter peaks (black) and TFAP2A enhancer peaks (red) on the y-axis. **(D)** Violin plots illustrating TFAP2A and IgG normalized reads (RPKM) at nucleosome depleted regions (ATAC-peaks) and at nucleosome occupied DNA (no ATAC-peak) **(E)** Density heatmap representing TFAP2A CUT&RUN and ATAC-seq profiles at TFAP2A peaks that overlap nucleosome depleted regions (ATAC-peaks) and at nucleosome bound DNA (no ATAC-peak), the number of TFAP2A peaks in each group are as labeled.

Figure S3: Example loci of TFAP2A peaks at open and closed chromatin. (A-B) IGV screenshots of TFAP2A peaks that **(A)** closed chromatin and **(B)** open chromatin, based on ATAC-seq, in SK-MEL-28 cells. Genes names and distance to a transcriptional start site as labeled. **(C)** HOMER motif analysis at TFAP2A peaks at closed chromatin and **(D)** at open chromatin. TF, transcription factors; the top ranking transcription factor motif is shown, with P-values calculated with HOMER-based hypergeometric enrichment analysis.

Figure S4: Generation of TFAP2A; TFAP2C double mutant SK-MEL-28 cell lines. (A) RNA-seq showing transcript counts of TFAP2 paralogs in SK-MEL-28 cells. Transcript counts for WT cells (n=4) and two *TFAP2A;TFAP2C* double knockout clones (4 replicates each) are shown. The expression of WT and mutant alleles of *TFAP2A* is comparable between cell lines whereas mutant alleles of *TFAP2C* are strongly reduced. **(B)** Two guide RNAs (crRNAs) each were designed to target exon 2 of *TFAP2A* and *TFAP2C* (yellow boxes). **(C)** A 401 base pair inversion and a 452 base pair deletion at exon 2 of *TFAP2A* and *TFAP2C*, respectively, was identified in clone 4.3. *TFAP2A* and *TFAP2C* mutant alleles resulted in a frame-shift and premature stop codon in alleles of both genes. **(D)** A 405 base pair deletion at exon 2 of *TFAP2A* resulted in a frame-shift and premature stop codon in clone 2.12. A 455 base pair deletion, and a 70 base pair insertion, 1 base pair deletion (Indel) was identified in exon 2 of *TFAP2C*. Such mutations resulted in a frame-shift and premature stop codon. Additional permutations were not identified at exon 2 of *TFAP2A* or *TFAP2C* in clone 4.3 or clone 2.12 cells. Inv; inversion, Del; deletion. **(E)** Western blot analysis confirming loss of TFAP2A and TFAP2C immunoactivity in clone 4.3 and clone 2.12 cell lines.

Figure S5: TFAP2 paralogs activate and inhibit gene expression directly. **(A)** Volcano plot illustrating differential gene expression as determined by RNA sequencing of *TFAP2*-KO cells (two independent clones (2.12 and 4.3); four replicates each) versus WT cells (SK-MEL-28; four replicates). Log2 fold change (FC) of mean transcript levels on the x-axis and log2 p-value on the y-axis. Red dots represent direct target genes of TFAP2A that are differentially expressed (FDR < 0.05, log2FC > |1|), as determined by anti-TFAP2 CUT&RUN in SK-MEL-28 cells.

Gray dots represent genes that are differentially expressed but not bound by TFAP2. The number and percentage of genes that are regulated by TFAP2 are specified. Directly TFAP2A-dependent genes were identified based on the gene-association rule (single nearest gene within 100 kb of a transcription start site).

Figure S6: TFAP2 paralogs directly activate and inhibit promoters as pioneer factors. (A-D) Screenshot of IGV genome browser (GRCH37/hg19), visualizing anti-TFAP2A CUT&RUN-seq (red), ATAC-seq (black), anti-H3K4Me3 CUT&RUN-seq (turquoise), anti-H3K27Ac CUT&RUN-seq (green) and RNA-seq (magenta) datasets at **(A-B)** TFAP2-activated promoters and **(C-D)** TFAP2-inhibited promoters. Genotypes as labeled; y-axes are grouped scaled per dataset. **(E-E'')** Violin plots representing **(E)** anti-H3K27Ac (two independent replicates) **(E')** ATAC-seq (four independent replicates) and **(E'')** anti-H3K4Me3 (two independent replicates) normalized reads at pioneered TFAP2-activated promoters. **(F-F'')** Violin plots representing **(F)** anti-H3K27Ac **(F')** ATAC-seq and **(E'')** anti-H3K4Me3 normalized reads at non-pioneered TFAP2-activated promoters. **(G-G'')** Violin plots representing **(G)** anti-H3K27Ac **(G')** ATAC-seq and **(G'')** anti-H3K4Me3 normalized reads at pioneered TFAP2-inhibited promoters. **(H-H'')** Violin plots representing **(H)** anti-H3K27Ac **(H')** ATAC-seq and **(H'')** anti-H3K4Me3 normalized reads at non-pioneered TFAP2-inhibited promoters. P-values shown were determined by Students t-test. **(I-L) H**ypergeometric analysis of TFAP2 regulated enhancers at TFAP2-activated (*) and TFAP2-inhibited (**) genes in *TFAP2*-KO cells (FDR < 0.05, |log2FC| > 1). The number of promoters in each category of TFAP2-regulated promoters is shown.

Figure S7: Additional examples of TFAP2-activated and -inhibited promoters. (A-B) Screenshots of IGV genome browser (GRCH37/hg19) visualizing anti-TFAP2A, anti-H3K4Me3, anti-H3K27Ac CUT&RUN-seq, ATAC-seq and RNA-seq profiles at **(A)** the TFAP2-activated *ZNF540* promoter and **(B)** the TFAP2-inhibited *S100A16* promoter. Genotypes as labeled; y-axes are grouped scaled per dataset.

Figure S8: TFAP2 paralogs modulate the binding of MITF. (A) Density heatmap centred on 9,413 peaks co-bound by TFAP2A and MITF, showing anti-TFAP2, anti-MITF, ATAC-seq, and anti-H3K27Ac CUT&RUN profiles in SK-MEL-28 cells.

Regions shown are +/- 5 kb from peak center. **(B)** Violin plot showing anti-MITF CUT&RUN signal (RPKM) in *TFAP2*-KO and SK-MEL-28 cells at loci not bound by TFAP2A. ns; non-significant by Students t-test. **(C)** Scatterplot of TFAP2-dependent MITF peaks showing log2 normalized reads on the x-axis and log2FC on the y-axis in *TFAP2*-KO versus WT cells. **(D)** Screenshots of IGV genome browser (GRCH37/hg19); genotypes as labeled, visualizing anti-TFAP2A and anti-MITF CUT&RUN-seq and ATAC-seq profiles at TFAP2-dependent MITF peaks, mutually dependent MITF/TFAP2 peaks and an example of a non-overlapping, TFAP2-independent MITF peak. **(E)** Volcano plot showing increased H3K27Me3 CUT&RUN signal at mutually dependent TFAP2/MITF peaks in *MITF*-KO cells versus WT cells. P-values were determined by Students t-test. Normalized reads (RPKM), **(F-G)** Screenshots of IGV genome browser (GRCH37/hg19), visualizing anti-H3K27Me3 CUT&RUN-seq profiles in *MIT*F-KO and WT cells. Peaks were called using MACS2 software (two independent replicates) and are illustrated by blue bars. Two examples loci of mutually dependent TFAP2/MITF peaks showing increased H3K27Me3 signals are shown, **(F)** at the *TRPM1* promoter and **(G)** at two *FRMD4B* enhancers. Mutually-dependent peaks are indicated by red arrows.

Figure S9: Density heatmap of TFAP2 regulated MITF peaks. Density heatmap centred on TFAP2 regulated MITF peaks (Top cluster) TFAP2-dependent MITF peaks, (Second cluster) Mutually dependent TFAP2/MITF peaks, (third cluster) TFAP2-inhibited MITF peaks and (forth cluster) independent peaks, showing two replicates of anti-MITF CUT&RUN in SK-MEL-28 and *TFAP2*-KO cells, and two replicates of anti-TFAP2A CUT&RUN in SK-MEL-28 and *MITF*-KO cells. Regions shown are +/- 5 kb from peak center.

Figure S10: TFAP2 and MITF do not co-inhibit enhancers at TFAP2-inhibited or MITF-inhibited genes in SK-MEL-28 cells. (A-A') Violin plot of TFAP2 dependent MITF peaks at TFAP2-inhibied enhancers (i.e. co-inhibited enhancers) showing **(B)** anti-MITF CUT&RUN and **(A')** ATAC-Seq profiles in *TFAP2*-KO and WT SK-MEL-28 cells. Such loci were not significantly enriched at MITF-inhibited or TFAP2-inhibited genes. (A'') Schematic of TFAP2/ MITF co-inhibited enhancers. In this example TFAP2 is a pioneer factor recruiting MITF, in its repressor form, to condense chromatin. Loss of TFAP2 in TFAP2-KO cells results in loss of MITF-repressor

binding and opening of chromatin by an alternative pioneer factor. **(B-B')** Violin plot of TFAP2-inhibited MITF peaks at modestly TFAP2-inhibted enhancers showing **(C)** anti-MITF CUT&RUN **(B')** ATAC-Seq profiles in *TFAP2*-KO and WT SK-MEL-28 cells. Such loci were not significantly enriched at MITF-inhibited or TFAP2-inhibited genes. (B'') Schematic of TFAP2-inhibted MITF peaks at modestly inhibited enhancers (Log2FC > -0.5 – -1). In this example TFAP2 recruits a repressor protein and inhibits MITF binding in WT cells. In the absence of TFAP2, MITF recruits SWI/SNF and opens chromatin via an alternative pioneer factor.

Figure S11: Genes that harbor TFAP2-independent anti-MITF peaks are enriched for cell cycle and DNA-repair. (A) Plot-profile showing MITF CUT&RUN peak signal at TFAP2-independent MITF peaks in *TFAP2*-KO and WT SK-MEL-28 cell lines. **(B)** Genes that harbor TFAP2-independent anti-MITF peaks were analyzed for enriched gene ontology biological process using GREAT (single nearest gene +/- 100kb).

Figure S12: Example of an TFAP2-dependent enhancer at intron 2 of MITF. Screenshot of IGV genome browser (GRCH37/hg19) visualizing anti-TFAP2A, ATAC-seq, anti-H3K27Ac and RNA-seq profiles at intron 2 of MITF. Dashed rectangle indicates an TFAP2-dependent NDR. MITF and downstream regions are shown, blue arrows indicate strand orientation and horizontal rectangles the exons. Genotypes are as labeled; y-axes are grouped scaled per dataset.

Figure S13: TFAP2 directly activates genes associated with cell differentiation and proliferation, and direct inhibits genes associated with cell adhesion and cell migration. (A-B) The top 55 genes that are directly TFAP2-activated and associated with the GO terms **(A)** cell differentiation and pigmentation and **(B)** proliferation are represented by heatmap (log2FC). **(C)** the top 55 genes that are directly TFAP2-inhibited and associated with the GO terms cell adhesion and cell migration are represented by heatmap (log2FC). C1: *TFAP2*-KO clone 4.3, C2: *TFAP2*-KO clone 2.12. **(D)** Wound healing scratch-recovery-assay over 24 hours in WT and *TFAP2*-KO cells. *TFAP2*-KO cells show reduced migration capacity compared to wild type SK-MEL-28 cells.

References cited:

Aras, S., Saladi, S.V., Basuroy, T., Marathe, H.G., Lores, P., de la Serna, I.L., 2019. BAF60A mediates interactions between the microphthalmia-associated transcription factor and the BRG1-containing SWI/SNF complex during melanocyte differentiation. J Cell Physiol 234, 11780-11791.

Atchison, M.L., 2014. Function of YY1 in Long-Distance DNA Interactions. Front Immunol 5, 45.

Bamforth, S.D., Braganca, J., Eloranta, J.J., Murdoch, J.N., Marques, F.I., Kranc, K.R., Farza, H., Henderson, D.J., Hurst, H.C., Bhattacharya, S., 2001. Cardiac malformations, adrenal agenesis, neural crest defects and exencephaly in mice lacking Cited2, a new Tfap2 co-activator. Nat Genet 29, 469-474.

Barrallo-Gimeno, A., Holzschuh, J., Driever, W., Knapik, E.W., 2004. Neural crest survival and differentiation in zebrafish depends on mont blanc/tfap2a gene function. Development 131, 1463-1477.

Baxter, L.L., Loftus, S.K., Pavan, W.J., 2009. Networks and pathways in pigmentation, health, and disease. Wiley Interdiscip Rev Syst Biol Med 1, 359-371.

Baxter, L.L., Watkins-Chow, D.E., Pavan, W.J., Loftus, S.K., 2019. A curated gene list for expanding the horizons of pigmentation biology. Pigment Cell Melanoma Res 32, 348-358.

Bejjani, F., Evanno, E., Zibara, K., Piechaczyk, M., Jariel-Encontre, I., 2019. The AP-1 transcriptional complex: Local switch or remote command? Biochim Biophys Acta Rev Cancer 1872, 11-23.

Betancur, P., Bronner-Fraser, M., Sauka-Spengler, T., 2010. Assembling neural crest regulatory circuits into a gene regulatory network. Annu Rev Cell Dev Biol 26, 581-603.

Braganca, J., Eloranta, J.J., Bamforth, S.D., Ibbitt, J.C., Hurst, H.C., Bhattacharya, S., 2003. Physical and functional interactions among AP-2 transcription factors, p300/CREB-binding protein, and CITED2. The Journal of biological chemistry 278, 16021-16029.

Brewer, S., Jiang, X., Donaldson, S., Williams, T., Sucov, H.M., 2002. Requirement for AP-2alpha in cardiac outflow tract morphogenesis. Mech Dev 110, 139-149.

Buenrostro, J.D., Giresi, P.G., Zaba, L.C., Chang, H.Y., Greenleaf, W.J., 2013. Transposition of native chromatin for fast and sensitive epigenomic profiling of open chromatin, DNA-binding proteins and nucleosome position. Nat Methods 10, 1213-1218.

Buenrostro, J.D., Wu, B., Chang, H.Y., Greenleaf, W.J., 2015. ATAC-seq: A Method for Assaying Chromatin Accessibility Genome-Wide. Curr Protoc Mol Biol 109, 21.29.21-21.29.29.

Campbell, N.R., Rao, A., Zhang, M., Baron, M., Heilmann, S., Deforet, M., Kenny, C., Ferretti, L., Huang, T.-H., Garg, M., Nsengimana, J., Montal, E., Tagore, M., Hunter, M., Newton-Bishop, J., Middleton, M.R., Corrie, P., Adams, D.J., Rabbie, R., Levesque, M.P., Cornell, R.A., Yanai, I., Xavier, J.B., White, R.M., 2021. Cell state diversity promotes metastasis through heterotypic cluster formation in melanoma. Developmental Cell, 2020.2008.2024.265140.

Carreira, S., Goodall, J., Denat, L., Rodriguez, M., Nuciforo, P., Hoek, K.S., Testori, A., Larue, L., Goding, C.R., 2006. Mitf regulation of Dia1 controls melanoma proliferation and invasiveness. Genes Dev 20, 3426-3439.

Creyghton, M.P., Cheng, A.W., Welstead, G.G., Kooistra, T., Carey, B.W., Steine, E.J., Hanna, J., Lodato, M.A., Frampton, G.M., Sharp, P.A., Boyer, L.A., Young, R.A., Jaenisch,

R., 2010. Histone H3K27ac separates active from poised enhancers and predicts developmental state. Proc Natl Acad Sci U S A 107, 21931-21936.

de la Serna, I.L., Ohkawa, Y., Higashi, C., Dutta, C., Osias, J., Kommajosyula, N., Tachibana, T., Imbalzano, A.N., 2006. The microphthalmia-associated transcription factor requires SWI/SNF enzymes to activate melanocyte-specific genes. J Biol Chem 281, 20233-20241.

Dilshat, R., Fock, V., Kenny, C., Gerritsen, I., Lasseur, R.M.J., Travnickova, J., Eichhoff, O.M., Cerny, P., Moller, K., Sigurbjornsdottir, S., Kirty, K., Einarsdottir, B.O., Cheng, P.F., Levesque, M., Cornell, R.A., Patton, E.E., Larue, L., de Tayrac, M., Magnusdottir, E., Helga Ogmundsdottir, M., Steingrimsson, E., 2021. MITF reprograms the extracellular matrix and focal adhesion in melanoma. Elife 10.

Dobin, A., Davis, C.A., Schlesinger, F., Drenkow, J., Zaleski, C., Jha, S., Batut, P., Chaisson, M., Gingeras, T.R., 2013. STAR: ultrafast universal RNA-seq aligner. Bioinformatics 29, 15-21.

Du, J., Li, L., Ou, Z., Kong, C., Zhang, Y., Dong, Z., Zhu, S., Jiang, H., Shao, Z., Huang, B., Lu, J., 2012. FOXC1, a target of polycomb, inhibits metastasis of breast cancer cells. Breast Cancer Res Treat 131, 65-73.

Eckert, D., Buhl, S., Weber, S., Jager, R., Schorle, H., 2005. The AP-2 family of transcription factors. Genome Biol 6, 246.

Fernandez Garcia, M., Moore, C.D., Schulz, K.N., Alberto, O., Donague, G., Harrison, M.M., Zhu, H., Zaret, K.S., 2019. Structural Features of Transcription Factors Associating with Nucleosome Binding. Mol Cell 75, 921-932 e926.

Goding, C.R., 2000. Mitf from neural crest to melanoma: signal transduction and transcription in the melanocyte lineage. Genes Dev 14, 1712-1728.

Grossman, S.R., Engreitz, J., Ray, J.P., Nguyen, T.H., Hacohen, N., Lander, E.S., 2018. Positional specificity of different transcription factor classes within enhancers. Proc Natl Acad Sci U S A 115, E7222-E7230.

Hartman, M.L., Czyz, M., 2015. MITF in melanoma: mechanisms behind its expression and activity. Cell Mol Life Sci 72, 1249-1260.

Higdon, C.W., Mitra, R.D., Johnson, S.L., 2013. Gene expression analysis of zebrafish melanocytes, iridophores, and retinal pigmented epithelium reveals indicators of biological function and developmental origin. PLoS One 8, e67801.

Hoek, K.S., Eichhoff, O.M., Schlegel, N.C., Döbbeling, U., Kobert, N., Schaerer, L., Hemmi, S., Dummer, R., 2008a. In vivo switching of human melanoma cells between proliferative and invasive states. Cancer Res 68, 650-656.

Hoek, K.S., Schlegel, N.C., Brafford, P., Sucker, A., Ugurel, S., Kumar, R., Weber, B.L., Nathanson, K.L., Phillips, D.J., Herlyn, M., Schadendorf, D., Dummer, R., 2006. Metastatic potential of melanomas defined by specific gene expression profiles with no BRAF signature. Pigment Cell Res 19, 290-302.

Hoek, K.S., Schlegel, N.C., Eichhoff, O.M., Widmer, D.S., Praetorius, C., Einarsson, S.O., Valgeirsdottir, S., Bergsteinsdottir, K., Schepsky, A., Dummer, R., Steingrimsson, E., 2008b. Novel MITF targets identified using a two-step DNA microarray strategy. Pigment Cell Melanoma Res 21, 665-676.

Huang, S., Jean, D., Luca, M., Tainsky, M.A., Bar-Eli, M., 1998. Loss of AP-2 results in downregulation of c-KIT and enhancement of melanoma tumorigenicity and metastasis. EMBO J 17, 4358-4369.

Jonsson, G., Busch, C., Knappskog, S., Geisler, J., Miletic, H., Ringner, M., Lillehaug, J.R., Borg, A., Lonning, P.E., 2010. Gene expression profiling-based identification of molecular subtypes in stage IV melanomas with different clinical outcome. Clin Cancer Res 16, 3356-3367.

Keenen, B., Qi, H., Saladi, S.V., Yeung, M., de la Serna, I.L., 2010. Heterogeneous SWI/SNF chromatin remodeling complexes promote expression of microphthalmia-associated transcription factor target genes in melanoma. Oncogene 29, 81-92.

Kim, S., Yu, N.K., Kaang, B.K., 2015. CTCF as a multifunctional protein in genome regulation and gene expression. Exp Mol Med 47, e166.

Knight, R.D., Javidan, Y., Nelson, S., Zhang, T., Schilling, T., 2004. Skeletal and pigment cell defects in the lockjaw mutant reveal multiple roles for zebrafish tfap2a in neural crest development. Dev Dyn 229, 87-98.

Knight, R.D., Nair, S., Nelson, S.S., Afshar, A., Javidan, Y., Geisler, R., Rauch, G.J., Schilling, T.F., 2003. lockjaw encodes a zebrafish tfap2a required for early neural crest development. Development 130, 5755-5768.

Kołat, D., Kałuzińska, Ż., Bednarek, A.K., Płuciennik, E., 2021. WWOX Loses the Ability to Regulate Oncogenic AP-2γ and Synergizes with Tumor Suppressor AP-2α in High-Grade Bladder Cancer. Cancers (Basel) 13.

Kuckenberg, P., Kubaczka, C., Schorle, H., 2012. The role of transcription factor Tcfap2c/TFAP2C in trophectoderm development. Reprod Biomed Online 25, 12-20.

Lang, D., Lu, M.M., Huang, L., Engleka, K.A., Zhang, M., Chu, E.Y., Lipner, S., Skoultchi, A., Millar, S.E., Epstein, J.A., 2005. Pax3 functions at a nodal point in melanocyte stem cell differentiation. Nature 433, 884-887.

Langmead, B., Salzberg, S.L., 2012. Fast gapped-read alignment with Bowtie 2. Nat Methods 9, 357-359.

Langmead, B., Trapnell, C., Pop, M., Salzberg, S.L., 2009. Ultrafast and memory-efficient alignment of short DNA sequences to the human genome. Genome Biol 10, R25.

Laurette, P., Strub, T., Koludrovic, D., Keime, C., Le Gras, S., Seberg, H., Van Otterloo, E., Imrichova, H., Siddaway, R., Aerts, S., Cornell, R.A., Mengus, G., Davidson, I., 2015. Transcription factor MITF and remodeller BRG1 define chromatin organisation at regulatory elements in melanoma cells. Elife 4.

Lee, B.K., Uprety, N., Jang, Y.J., Tucker, S.K., Rhee, C., LeBlanc, L., Beck, S., Kim, J., 2018. Fosl1 overexpression directly activates trophoblast-specific gene expression programs in embryonic stem cells. Stem Cell Res 26, 95-102.

Leroy, B., Girard, L., Hollestelle, A., Minna, J.D., Gazdar, A.F., Soussi, T., 2014. Analysis of TP53 mutation status in human cancer cell lines: a reassessment. Hum Mutat 35, 756-765.

Li, L., Wang, Y., Torkelson, J.L., Shankar, G., Pattison, J.M., Zhen, H.H., Fang, F., Duren, Z., Xin, J., Gaddam, S., Melo, S.P., Piekos, S.N., Li, J., Liaw, E.J., Chen, L., Li, R., Wernig, M., Wong, W.H., Chang, H.Y., Oro, A.E., 2019. TFAP2C- and p63-Dependent Networks Sequentially Rearrange Chromatin Landscapes to Drive Human Epidermal Lineage Commitment. Cell Stem Cell 24, 271-284 e278.

Li, W., Cornell, R.A., 2007. Redundant activities of Tfap2a and Tfap2c are required for neural crest induction and development of other non-neural ectoderm derivatives in zebrafish embryos. Dev Biol 304, 338-354.

Lin, C.Y., Chao, A., Wang, T.H., Lee, L.Y., Yang, L.Y., Tsai, C.L., Wang, H.S., Lai, C.H., 2016. Nucleophosmin/B23 is a negative regulator of estrogen receptor alpha expression via AP2gamma in endometrial cancer cells. Oncotarget 7, 60038-60052.

Liu, H., Duncan, K., Helverson, A., Kumari, P., Mumm, C., Xiao, Y., Carlson, J.C., Darbellay, F., Visel, A., Leslie, E., Breheny, P., Erives, A.J., Cornell, R.A., 2020. Analysis of zebrafish periderm enhancers facilitates identification of a regulatory variant near human KRT8/18. Elife 9.

Liu, H., Tan, B.C., Tseng, K.H., Chuang, C.P., Yeh, C.W., Chen, K.D., Lee, S.C., Yung, B.Y., 2007. Nucleophosmin acts as a novel AP2alpha-binding transcriptional corepressor during cell differentiation. EMBO Rep 8, 394-400.

1249 Love, M.I., Huber, W., Anders, S., 2014. Moderated estimation of fold change and dispersion
1250 for RNA-seq data with DESeq2. Genome Biol 15, 550.
1251 Luo, T., Matsuo-Takasaki, M., Thomas, M.L., Weeks, D.L., Sargent, T.D., 2002.
1252 Transcription factor AP-2 is an essential and direct regulator of epidermal development in
1253 Xenopus. Dev Biol 245, 136-144.
1254 Mavrothalassitis, G., Ghysdael, J., 2000. Proteins of the ETS family with transcriptional
1255 repressor activity. Oncogene 19, 6524-6532.
1256 Mayran, A., Khetchoumian, K., Hariri, F., Pastinen, T., Gauthier, Y., Balsalobre, A., Drouin,
1257 J., 2018. Pioneer factor Pax7 deploys a stable enhancer repertoire for specification of cell
1258 fate. Nat Genet 50, 259-269.
1259 McLean, C.Y., Bristor, D., Hiller, M., Clarke, S.L., Schaar, B.T., Lowe, C.B., Wenger, A.M.,
1260 Bejerano, G., 2010. GREAT improves functional interpretation of cis-regulatory regions. Nat
1261 Biotechnol 28, 495-501.
1262 Meers, M.P., Bryson, T.D., Henikoff, J.G., Henikoff, S., 2019. Improved CUT&RUN
1263 chromatin profiling tools. Elife 8.
1264 Mi, H., Ebert, D., Muruganujan, A., Mills, C., Albou, L.P., Mushayamaha, T., Thomas, P.D.,
1265 2021. PANTHER version 16: a revised family classification, tree-based classification tool,
1266 enhancer regions and extensive API. Nucleic Acids Res 49, D394-d403.
1267 Miller, J.C., Holmes, M.C., Wang, J., Guschin, D.Y., Lee, Y.L., Rupniewski, I., Beausejour,
1268 C.M., Waite, A.J., Wang, N.S., Kim, K.A., Gregory, P.D., Pabo, C.O., Rebar, E.J., 2007. An
1269 improved zinc-finger nuclease architecture for highly specific genome editing. Nat
1270 Biotechnol 25, 778-785.
1271 Mitchell, P.J., Timmons, P.M., Hebert, J.M., Rigby, P.W., Tjian, R., 1991. Transcription
1272 factor AP-2 is expressed in neural crest cell lineages during mouse embryogenesis. Genes
1273 Dev 5, 105-119.
1274 Mollaaghababa, R., Pavan, W.J., 2003. The importance of having your SOX on: role of
1275 SOX10 in the development of neural crest-derived melanocytes and glia. Oncogene 22, 3024-
1276 3034.
1277 Moser, M., Ruschoff, J., Buettner, R., 1997. Comparative analysis of AP-2 alpha and AP-2
1278 beta gene expression during murine embryogenesis. Developmental Dynamics 208, 115-124.
1279 Pastor, W.A., Liu, W., Chen, D., Ho, J., Kim, R., Hunt, T.J., Lukianchikov, A., Liu, X., Polo,
1280 J.M., Jacobsen, S.E., Clark, A.T., 2018. TFAP2C regulates transcription in human naive
1281 pluripotency by opening enhancers. Nat Cell Biol 20, 553-564.
1282 Pekowska, A., Benoukraf, T., Zacarias-Cabeza, J., Belhocine, M., Koch, F., Holota, H.,
1283 Imbert, J., Andrau, J.C., Ferrier, P., Spicuglia, S., 2011. H3K4 tri-methylation provides an
1284 epigenetic signature of active enhancers. EMBO J 30, 4198-4210.
1285 Petruk, S., Cai, J., Sussman, R., Sun, G., Kovermann, S.K., Mariani, S.A., Calabretta, B.,
1286 McMahon, S.B., Brock, H.W., Iacovitti, L., Mazo, A., 2017. Delayed Accumulation of
1287 H3K27me3 on Nascent DNA Is Essential for Recruitment of Transcription Factors at Early
1288 Stages of Stem Cell Differentiation. Mol Cell 66, 247-257 e245.
1289 Pihlajamaa, P., Sahu, B., Lyly, L., Aittomaki, V., Hautaniemi, S., Janne, O.A., 2014. Tissue-
1290 specific pioneer factors associate with androgen receptor cistromes and transcription
1291 programs. EMBO J 33, 312-326.
1292 Praetorius, C., Grill, C., Stacey, S.N., Metcalf, A.M., Gorkin, D.U., Robinson, K.C., Van
1293 Otterloo, E., Kim, R.S., Bergsteinsdottir, K., Ogmundsdottir, M.H., Magnusdottir, E., Mishra,
1294 P.J., Davis, S.R., Guo, T., Zaidi, M.R., Helgason, A.S., Sigurdsson, M.I., Meltzer, P.S.,
1295 Merlino, G., Petit, V., Larue, L., Loftus, S.K., Adams, D.R., Sobhiafshar, U., Emre, N.C.,
1296 Pavan, W.J., Cornell, R., Smith, A.G., McCallion, A.S., Fisher, D.E., Stefansson, K., Sturm,
1297 R.A., Steingrimsson, E., 2013. A polymorphism in IRF4 affects human pigmentation through
1298 a tyrosinase-dependent MITF/TFAP2A pathway. Cell 155, 1022-1033.

Rambow, F., Job, B., Petit, V., Gesbert, F., Delmas, V., Seberg, H., Meurice, G., Van Otterloo, E., Dessen, P., Robert, C., Gautheret, D., Cornell, R.A., Sarasin, A., Larue, L., 2015. New Functional Signatures for Understanding Melanoma Biology from Tumor Cell Lineage-Specific Analysis. Cell Rep 13, 840-853.

Rambow, F., Marine, J.C., Goding, C.R., 2019. Melanoma plasticity and phenotypic diversity: therapeutic barriers and opportunities. Genes Dev 33, 1295-1318.

Rambow, F., Rogiers, A., Marin-Bejar, O., Aibar, S., Femel, J., Dewaele, M., Karras, P., Brown, D., Chang, Y.H., Debiec-Rychter, M., Adriaens, C., Radaelli, E., Wolter, P., Bechter, O., Dummer, R., Levesque, M., Piris, A., Frederick, D.T., Boland, G., Flaherty, K.T., van den Oord, J., Voet, T., Aerts, S., Lund, A.W., Marine, J.C., 2018. Toward Minimal Residual Disease-Directed Therapy in Melanoma. Cell 174, 843-855 e819.

Ramírez, F., Ryan, D.P., Grüning, B., Bhardwaj, V., Kilpert, F., Richter, A.S., Heyne, S., Dündar, F., Manke, T., 2016. deepTools2: a next generation web server for deep-sequencing data analysis. Nucleic Acids Res 44, W160-165.

Ringrose, L., Paro, R., 2004. Epigenetic regulation of cellular memory by the Polycomb and Trithorax group proteins. Annu Rev Genet 38, 413-443.

Ross-Innes, C.S., Stark, R., Teschendorff, A.E., Holmes, K.A., Ali, H.R., Dunning, M.J., Brown, G.D., Gojis, O., Ellis, I.O., Green, A.R., Ali, S., Chin, S.F., Palmieri, C., Caldas, C., Carroll, J.S., 2012. Differential oestrogen receptor binding is associated with clinical outcome in breast cancer. Nature 481, 389-393.

Sander, J.D., Dahlborg, E.J., Goodwin, M.J., Cade, L., Zhang, F., Cifuentes, D., Curtin, S.J., Blackburn, J.S., Thibodeau-Beganny, S., Qi, Y., Pierick, C.J., Hoffman, E., Maeder, M.L., Khayter, C., Reyon, D., Dobbs, D., Langenau, D.M., Stupar, R.M., Giraldez, A.J., Voytas, D.F., Peterson, R.T., Yeh, J.R., Joung, J.K., 2011. Selection-free zinc-finger-nuclease engineering by context-dependent assembly (CoDA). Nat Methods 8, 67-69.

Sander, J.D., Maeder, M.L., Reyon, D., Voytas, D.F., Joung, J.K., Dobbs, D., 2010. ZiFiT (Zinc Finger Targeter): an updated zinc finger engineering tool. Nucleic Acids Res 38, W462-468.

Schorle, H., Meier, P., Buchert, M., Jaenisch, R., Mitchell, P.J., 1996. Transcription factor AP-2 essential for cranial closure and craniofacial development. Nature 381, 235-238.

Seberg, H.E., Van Otterloo, E., Cornell, R.A., 2017a. Beyond MITF: Multiple transcription factors directly regulate the cellular phenotype in melanocytes and melanoma. Pigment Cell Melanoma Res 30, 454-466.

Seberg, H.E., Van Otterloo, E., Loftus, S.K., Liu, H., Bonde, G., Sompallae, R., Gildea, D.E., Santana, J.F., Manak, J.R., Pavan, W.J., Williams, T., Cornell, R.A., 2017b. TFAP2 paralogs regulate melanocyte differentiation in parallel with MITF. PLoS Genet 13, e1006636.

Sekiya, T., Zaret, K.S., 2007. Repression by Groucho/TLE/Grg proteins: genomic site recruitment generates compacted chromatin in vitro and impairs activator binding in vivo. Mol Cell 28, 291-303.

Sherwood, R.I., Hashimoto, T., O'Donnell, C.W., Lewis, S., Barkal, A.A., van Hoff, J.P., Karun, V., Jaakkola, T., Gifford, D.K., 2014. Discovery of directional and nondirectional pioneer transcription factors by modeling DNase profile magnitude and shape. Nat Biotechnol 32, 171-178.

Skene, P.J., Henikoff, S., 2017. An efficient targeted nuclease strategy for high-resolution mapping of DNA binding sites. Elife 6.

Strub, T., Giuliano, S., Ye, T., Bonet, C., Keime, C., Kobi, D., Le Gras, S., Cormont, M., Ballotti, R., Bertolotto, C., Davidson, I., 2011. Essential role of microphthalmia transcription factor for DNA replication, mitosis and genomic stability in melanoma. Oncogene 30, 2319-2332.

1348 Swinstead, E.E., Miranda, T.B., Paakinaho, V., Baek, S., Goldstein, I., Hawkins, M.,
1349 Karpova, T.S., Ball, D., Mazza, D., Lavis, L.D., Grimm, J.B., Morisaki, T., Grontved, L.,
1350 Presman, D.M., Hager, G.L., 2016a. Steroid Receptors Reprogram FoxA1 Occupancy
1351 through Dynamic Chromatin Transitions. Cell 165, 593-605.
1352 Swinstead, E.E., Paakinaho, V., Presman, D.M., Hager, G.L., 2016b. Pioneer factors and
1353 ATP-dependent chromatin remodeling factors interact dynamically: A new perspective:
1354 Multiple transcription factors can effect chromatin pioneer functions through dynamic
1355 interactions with ATP-dependent chromatin remodeling factors. Bioessays 38, 1150-1157.
1356 Tan, C.C., Sindhu, K.V., Li, S., Nishio, H., Stoller, J.Z., Oishi, K., Puttreddy, S., Lee, T.J.,
1357 Epstein, J.A., Walsh, M.J., Gelb, B.D., 2008. Transcription factor Ap2delta associates with
1358 Ash2l and ALR, a trithorax family histone methyltransferase, to activate Hoxc8 transcription.
1359 Proc Natl Acad Sci U S A 105, 7472-7477.
1360 Tan, S.K., Lin, Z.H., Chang, C.W., Varang, V., Chng, K.R., Pan, Y.F., Yong, E.L., Sung,
1361 W.K., Cheung, E., 2011. AP-2gamma regulates oestrogen receptor-mediated long-range
1362 chromatin interaction and gene transcription. EMBO J 30, 2569-2581.
1363 Tirosh, I., Izar, B., Prakadan, S.M., Wadsworth, M.H., 2nd, Treacy, D., Trombetta, J.J.,
1364 Rotem, A., Rodman, C., Lian, C., Murphy, G., Fallahi-Sichani, M., Dutton-Regester, K., Lin,
1365 J.R., Cohen, O., Shah, P., Lu, D., Genshaft, A.S., Hughes, T.K., Ziegler, C.G., Kazer, S.W.,
1366 Gaillard, A., Kolb, K.E., Villani, A.C., Johannessen, C.M., Andreev, A.Y., Van Allen, E.M.,
1367 Bertagnolli, M., Sorger, P.K., Sullivan, R.J., Flaherty, K.T., Frederick, D.T., Jane-Valbuena,
1368 J., Yoon, C.H., Rozenblatt-Rosen, O., Shalek, A.K., Regev, A., Garraway, L.A., 2016.
1369 Dissecting the multicellular ecosystem of metastatic melanoma by single-cell RNA-seq.
1370 Science 352, 189-196.
1371 Tsoi, J., Robert, L., Paraiso, K., Galvan, C., Sheu, K.M., Lay, J., Wong, D.J.L., Atefi, M.,
1372 Shirazi, R., Wang, X., Braas, D., Grasso, C.S., Palaskas, N., Ribas, A., Graeber, T.G., 2018.
1373 Multi-stage Differentiation Defines Melanoma Subtypes with Differential Vulnerability to
1374 Drug-Induced Iron-Dependent Oxidative Stress. Cancer Cell 33, 890-904 e895.
1375 Van Otterloo, E., Li, W., Bonde, G., Day, K.M., Hsu, M.Y., Cornell, R.A., 2010.
1376 Differentiation of zebrafish melanophores depends on transcription factors AP2 alpha and
1377 AP2 epsilon. PLoS Genet 6.
1378 Van Otterloo, E., Li, W., Garnett, A., Cattell, M., Medeiros, D.M., Cornell, R.A., 2012.
1379 Novel Tfap2-mediated control of soxE expression facilitated the evolutionary emergence of
1380 the neural crest. Development 139, 720-730.
1381 Verfaillie, A., Imrichova, H., Atak, Z.K., Dewaele, M., Rambow, F., Hulselmans, G.,
1382 Christiaens, V., Svetlichnyy, D., Luciani, F., Van den Mooter, L., Claerhout, S., Fiers, M.,
1383 Journe, F., Ghanem, G.E., Herrmann, C., Halder, G., Marine, J.C., Aerts, S., 2015. Decoding
1384 the regulatory landscape of melanoma reveals TEADS as regulators of the invasive cell state.
1385 Nat Commun 6, 6683.
1386 Vierbuchen, T., Ling, E., Cowley, C.J., Couch, C.H., Wang, X., Harmin, D.A., Roberts,
1387 C.W.M., Greenberg, M.E., 2017. AP-1 Transcription Factors and the BAF Complex Mediate
1388 Signal-Dependent Enhancer Selection. Mol Cell 68, 1067-1082.e1012.
1389 Voss, T.C., Hager, G.L., 2014. Dynamic regulation of transcriptional states by chromatin and
1390 transcription factors. Nat Rev Genet 15, 69-81.
1391 Wang, X., Bolotin, D., Chu, D.H., Polak, L., Williams, T., Fuchs, E., 2006. AP-2alpha: a
1392 regulator of EGF receptor signaling and proliferation in skin epidermis. J Cell Biol 172, 409-
1393 421.
1394 Wang, X., Pasolli, H.A., Williams, T., Fuchs, E., 2008. AP-2 factors act in concert with
1395 Notch to orchestrate terminal differentiation in skin epidermis. J Cell Biol 183, 37-48.
1396 Watts, J.A., Zhang, C., Klein-Szanto, A.J., Kormish, J.D., Fu, J., Zhang, M.Q., Zaret, K.S.,
1397 2011. Study of FoxA pioneer factor at silent genes reveals Rfx-repressed enhancer at Cdx2

and a potential indicator of esophageal adenocarcinoma development. PLoS Genet 7, e1002277.

White, J.R., Thompson, D.T., Koch, K.E., Kiriazov, B.S., Beck, A.C., van der Heide, D.M., Grimm, B.G., Kulak, M.V., Weigel, R.J., 2021. AP-2alpha-mediated activation of E2F and EZH2 drives melanoma metastasis. Cancer Res.

Wilson, B.G., Wang, X., Shen, X., McKenna, E.S., Lemieux, M.E., Cho, Y.J., Koellhoffer, E.C., Pomeroy, S.L., Orkin, S.H., Roberts, C.W., 2010. Epigenetic antagonism between polycomb and SWI/SNF complexes during oncogenic transformation. Cancer Cell 18, 316-328.

Wong, P.P., Miranda, F., Chan, K.V., Berlato, C., Hurst, H.C., Scibetta, A.G., 2012. Histone demethylase KDM5B collaborates with TFAP2C and Myc to repress the cell cycle inhibitor p21(cip) (CDKN1A). Mol Cell Biol 32, 1633-1644.

Yu, G., Wang, L.G., Han, Y., He, Q.Y., 2012. clusterProfiler: an R package for comparing biological themes among gene clusters. Omics 16, 284-287.

Zaret, K.S., 2020. Pioneer Transcription Factors Initiating Gene Network Changes. Annu Rev Genet 54, 367-385.

Zaret, K.S., Carroll, J.S., 2011. Pioneer transcription factors: establishing competence for gene expression. Genes Dev 25, 2227-2241.

Zhang, Y., Liu, T., Meyer, C.A., Eeckhoute, J., Johnson, D.S., Bernstein, B.E., Nusbaum, C., Myers, R.M., Brown, M., Li, W., Liu, X.S., 2008. Model-based analysis of ChIP-Seq (MACS). Genome Biol 9, R137.